

# Chapter 9

## Potential Applications of Carbon Nanotube Arrays

Besides the above applications described in Chap. 8, there are additional potential applications of CNT arrays which are relatively further away from commercialization and major progresses are still needed. We talk about these applications altogether in this chapter.

### 9.1 Mechanical Devices

CNTs possess extremely high tensile strengths. The yield strength of SWCNTs exceeds 45 GPa [1] with an average strength of 30 GPa [2], over 20 times the yield strength of typical high strength steels. The highest tensile strength of an individual MWCNT has been recorded to be 63 GPa. The measured Youngs modulus of SWCNTs is over 1 TPa [2, 3], lower than that of MWCNTs 1.3 TPa [4] or 1.8 TPa [5]. The strain at tensile failure has been measured to be as high as 5.3 % for SWCNTs [2] and 12 % for MWCNTs [6] at room temperature. The theoretical yield strain is up to 9 % or higher [7, 8] for defect-free SWCNTs. The unique strength and flexibility of CNTs make them potentially useful in many mechanical applications, ranging from everyday items such as clothes and sport gears to fictional combat jackets and space elevators. The aligned CNT ropes, CNT sheets, and aligned CNT composites would preserve the superb mechanical properties of the individual CNTs.

There are two kinds of aligned CNT materials used for mechanical devices. One kind is aligned CNT composites where the CNTs are used as additive and embedded in a matrix. Such aligned CNTs are usually fabricated by *ex situ* methods discussed in Sect. 6.2. After CNTs are synthesized as described in Chap. 3, CNTs are collected, purified if needed, and mixed with polymeric, ceramic, or other materials. In order to improve the dispersion of CNTs in the processing composites, the surfaces of CNTs are chemically functionalized or some surfactants are used as a dispersing agent. If the CNTs are randomly dispersed in the matrix, the mechanical properties of such composites are slightly enhanced. For example, random CNTs have been employed

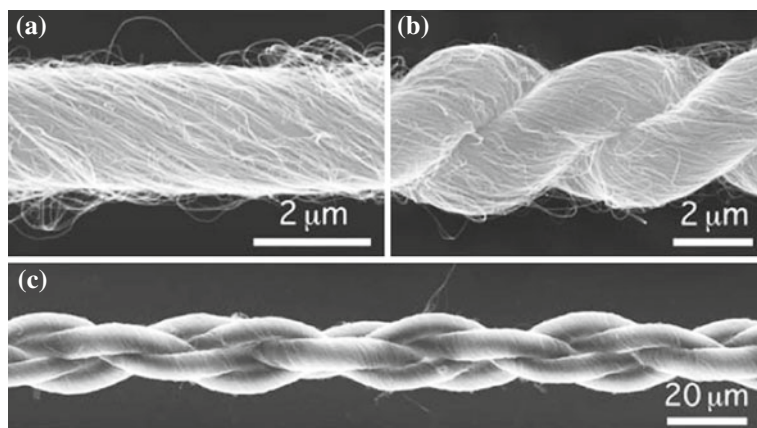


**Fig. 9.1** SEM images of polymer-free CNT ropes. **a** Single-ply MWCNT rope. **b** Two-ply MWCNT rope. **c** Four-ply MWCNT rope. From Zhang et al. [24]. Copyright (2004), AAAS

to enhance the mechanical strength of swords [9, 10]. In order to align the CNTs in the matrix, force fields, [11–15], magnetic fields [16], or electric fields [17–22] are applied on the liquid-like mixture. CNTs are aligned along a certain direction. The alignment methods for CNTs in matrices were reviewed [23] and discussed in Sect. 6.2.

Another is the aligned CNTs without matrices. The aligned CNTs can be synthesized first and then mechanically aligned to achieve an ordered structure, such as CNT ropes, CNT clothes, CNT films, etc. The details of the alignment methods are discussed in Sect. 6.2.3.2. The aligned CNTs can also be in situ grown directly on a substrate (see Sect. 6.1).

In this subchapter, we talk about the potential mechanical applications of both kinds of aligned CNT materials.

### 9.1.1 Carbon Nanotube Ropes

The CNT ropes are usually fabricated by spinning methods, including the wet-spinning method and the dry-spinning methods, as described in Sect. 6.2.3.2. The mechanical properties of these CNT ropes or bundles are reviewed recently [25].

Experimental data indicate that the mechanical properties of CNT ropes are lower than those of the individual CNTs. The CNTs in ropes are aligned parallel to one another [24] or twisted [26]. In the untwisted ropes, the CNTs are held together by van der Waals interactions and the untwisted ropes tensile strength is so weak that the rope breaks once the untwisted ropes are pulled [26]. So the CNT ropes are usually twisted to increase the strength [26]. The twisted pure CNT ropes can be fabricated by wet-spinning from CNT solvents [27] or dry-spinning directly from CVD-grown

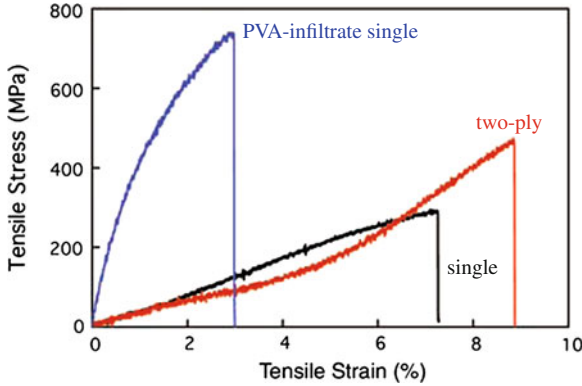


**Fig. 9.2** Stress–strain curves of single-ply (black), two-ply (red), and PVA-infiltrated single-ply (blue) ropes at a strain rate of 1% min for a centimeter gauge length. From Zhang et al. [24]. Copyright (2004), AAAS

CNTs [26, 28]. The fabrication details are discussed in Sect. 6.2.3.2. Figure 9.1 shows MWCNT ropes prepared by the dry-spinning method from CVD-synthesized CNT forests. Its stress–strain curve is shown in Fig. 9.2.

Detailed experimental results indicate that the CNTs in the twisted ropes are arranged in a helical structure [29]. The mechanical properties of CNT helical ropes depend on the microstructure of the ropes, such as the helix angle and the frictional force between CNTs. The tensile strength of twisted CNT ropes,  $\sigma_{\text{rope}}$ , follows the mechanical properties of textile fiber yarns [26, 29] and can be expressed as [30]

$$\sigma_{\text{rope}} \approx \sigma_{\text{CNT}} \cos^2 \alpha \left[ 1 - \frac{\sqrt{dQ/u}}{2L} \cos \alpha \right] \tag{9.1}$$

where  $\sigma_{\text{CNT}}$  is the tensile strength of the CNT,  $\alpha$  the helix angle that CNTs make with the rope axis,  $d$  the CNT diameter,  $L$  the CNT length,  $Q$  the CNT migration length, and  $u$  the friction coefficient between the CNTs. The CNTs in the twisted rope are inclined at the angle  $\alpha$  with respect to the tensile axis. The tensile strength decreases with the helix angle  $\alpha$  [29] according to Eq. 9.1. For short CNTs, however, there is little strength in the absence of twist because there are no significant transverse forces to bind the CNT assembly together. The transverse forces are generated by transfer of the tensile load to the rope surface, which locks the fibers together forming a coherent structure [26]. The tensile strength of a twisted rope increases with increasing coefficient of friction between CNTs, with CNT length, and with decreasing CNT diameter and CNT migration length.

Figure 9.3 shows Youngs modulus of CNT ropes with different diameters. Both experimental data [31] and theoretical analysis [32] indicate that the tensile modulus depends strongly on the diameter of the CNT ropes because of the creeping

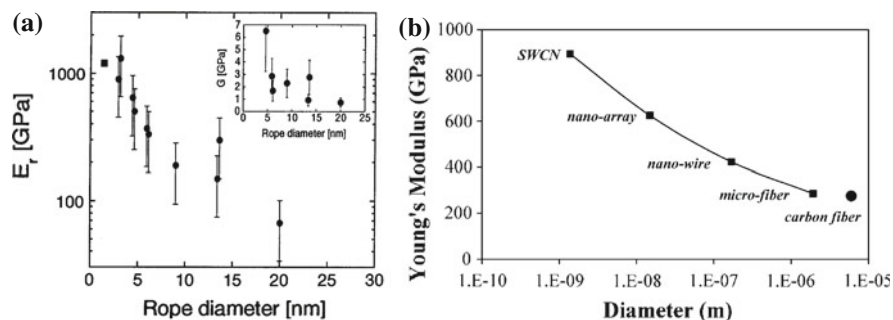


**Fig. 9.3** Young's modulus of SWCNT ropes with helical array geometry. **a** Experimental data and **b** theoretical data. **a** From Salvetat et al. [31]. Copyright (1999), American Physical Society. **b** From Pipes and Hubert [32]. Copyright (2003), American Chemical Society

between CNTs. With the increase in rope diameters, Young's modulus is diminished by approximately 68% when upscaling from nanoscale to microscale.

In order to increase the friction between CNTs, CNTs can be embedded in a polymer with high strength and high modulus like polyvinyl alcohol (PVA). The CNT/polymer ropes can be fabricated by wet-spinning or dry-spinning followed by soaking in a polymer solution. The tensile strength of SWCNT/PVA yarns increases to 850 MPa from 150 to 300 MPa of PVA-free yarns. The strength is still much lower than that of individual SWCNTs. Creep is a major problem for these CNT composite ropes.

The highest Young's modulus of the helical SWCNT ropes is about 15 GPa [33] for CNT ropes spun from coagulation solution (polymer is removed and CNT ropes mainly consist of CNTs), with a yield stress of 8.8 GPa. The highest stiffness is 357 GPa for CNT ropes spun directly from an aerogel CNTs [34]. The reported highest tensile strength is 150–300 MPa for MWCNT ropes fabricated directly from CNT forests [26]. The tensile strength is higher than most of commercial high-performance fibers while still more than an order of magnitude lower than the intrinsic modulus of individual SWCNTs of 37 GPa.

Twisted polymer fibers consisting of CNTs at less than 10 wt% have also been fabricated. The mechanical strength and modulus are enhanced compared with pure polymer fibers [13]. It is reported that the tensile strength and Young's modulus have reached 4.2 and 167 GPa, respectively, in the dry-jet wet-spinning poly(*p*-phenylene benzobisoxazole)/SWCNT ropes (SWCNT: 10 wt%) [35]. When the SWCNTs are lower than 2.1 wt%, the additive of SWCNTs does not enhance the mechanical properties [36].

In order to avoid creeping, two-ply ropes are fabricated by over-twisting a single rope (Fig. 9.1b), and four-ply ropes by oppositely twisting a two-ply rope (Fig. 9.1c), and even knitted or knotted ropes are fabricated [24]. Higher tensile strength values of 250–460 MPa are measured for two-ply yarns, while only 150–300 MPa for single-ply yarns (Fig. 9.2).

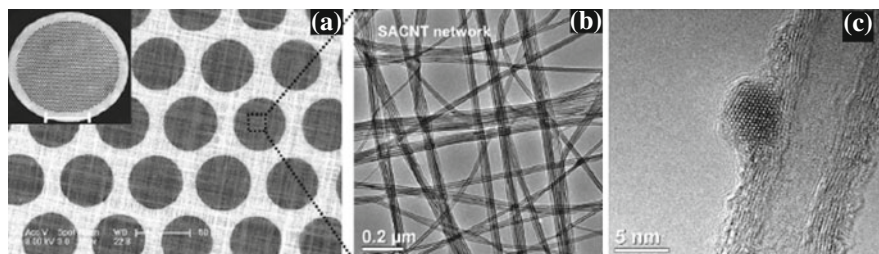


**Fig. 9.4** Morphologies of a TEM grid with CNT sheet as a supporting film. **a** SEM image of the CNT sheet over the holes of a copper grid. Inset: optical image of the coated TEM grid with a diameter of 3 mm. **b** TEM image of the CNT sheet covering a hole showing a network morphology. **c** HRTEM image of a Cu<sub>2</sub>S nanoparticle on one side of a nanotube of the TEM grid. From Zhang et al. [41]. Copyright (2008) American Chemical Society

Recent experimental data indicate that the parameters of the nanotubes, such as tube diameter, CNT wall thickness, tube length, and level of defects, play a more important role in the mechanical properties of the fibers than the initial tube arrangement do [37]. To improve the fiber strength, as well as the modulus, the tubes must be long and have a small diameter and thin walls.

### 9.1.2 TEM Grids

The continuous CNT sheets with centimeters in width and tens of nanometers in thickness can be fabricated by spinning methods [24, 28, 38] as described in Sect. 6.2.3.2. The CNTs are parallel-aligned in the drawing direction and end-to-end joined to form a continuous thin film, having a much better alignment than the as-synthesized CNT arrays [38]. These aligned CNT sheets are transparent and highly conductive [38–40], as a good candidate for TEM grid supporting films.

Figure 9.4 shows the morphologies of a TEM grid. In the fabrication of TEM grids, four layers of CNT thin sheets are directly cross-stacked layer by layer on TEM copper grids, then an organic solvent is dispensed on the sheets to bond the sheets onto the copper grid, following a CNT sheet cutting by a focused laser beam. The ultrathin CNT sheets cover the copper grid and regular networks with numerous holes are formed. The holes are mostly less than 1 μm in diameter, and the nanometer-sized holes are more than 60% of all holes. Considering the good electrical conductivity and mechanical strength of CNTs, these TEM grids are ideal tools for the characterization of nanomaterials [41]. The fine structures of individual nanoparticles can be clearly observed on HRTEM (Fig. 9.4c) when the nanoparticles are attached to a CNT on TEM grids.

In comparison with conventional TEM holey carbon grids, the TEM grids with CNT sheets have some advanced characteristics resulting from the excellent intrinsic physical properties of CNTs [41]. First, the CNT has strong adsorbability to adsorb

small nanoparticles and ensure them to be suspended stably during TEM observation. Second, due to good electrical conductivity of MWCNTs, the CNT sheet also has good electrical conductivity (bulk resistivity is about  $3.8 \times 10^{-4} \Omega\text{m}$ ). Third, because of the fixed interspace between sidewalls of the MWCNTs, i.e.,  $\sim 0.34 \text{ nm}$ , the CNT grid can be a standard sample for calibration of HRTEM magnification and size measurement of nanoparticles. In addition, the CNT sheets have better thermal stability than that of the conventional amorphous carbon film.

### 9.1.3 Artificial Setae

Replicating the multiscale structure of micron-size setae and nanometer-size spatulas of gecko lizard feet using microfabricated MWCNTs, CNT arrays can translate weak van der Waals interactions into enormous attractive forces [42]. The CNT block arrays ( $50\text{--}500 \mu\text{m}$  patches) are synthesized from photolithographic patterns. Each block array works as micron-size setae and consists of thousands of individual MWCNTs, the nano-sized spatulas. These patterned CNT arrays can stick to both hydrophobic and hydrophilic surfaces with a maximum shear stress of  $36 \text{ N/cm}^2$ , nearly four times higher than the gecko foot and 10 times higher than polymer pillars. The shear forces supported by the patterned CNT arrays are very stable and time independent.

### 9.1.4 Piezoresistive Effects: Pressure and Strain Sensors

MWCNT arrays are also very effective sensing element for pressure and strain sensors operating at elevated temperature [43]. When a CNT array is compressed, individual carbon nanotube starts to buckle, which in turn decreases the array's electrical resistance. The behavior is almost fully recoverable because of the high elasticity of the covalent carbon-carbon bond. The MWCNT array exhibits a significant increase in the change of resistance with increasing temperature of  $20\text{--}80^\circ\text{C}$ .

Experimental data of SWCNT arrays show that the normalized resistance changes in response to the changes in strain [44]. The resistance ratio  $\Delta R/R$  increases linearly with the strain, with a linearity of 0.991. The gauge factor, ratio of normalized change in piezoresistance to the change of strain, calculated from  $(\Delta R/R)/\varepsilon$  or  $(I_0 - I)/(I\varepsilon)$  (where  $I$  is the current and  $\varepsilon$  is the strain), is 248. Figure 9.5 plots the dynamic response of the sensor device at a frequency of 0.1 Hz for three different strain intervals. When the strain of the suspended SWCNT array is located in the scope of  $0.0267\text{--}0.0497$  and  $0.0450\text{--}0.0769\%$ , the response curve reveals separate top-flat and bottom-flat appearances. A perfect triangular wave shows the strain in the linear changes in the rate of resistance ( $\Delta R/R$ ) as a response to the changes in strain. Such SWCNT array devices with high sensitivity have potential application as strain gauges.

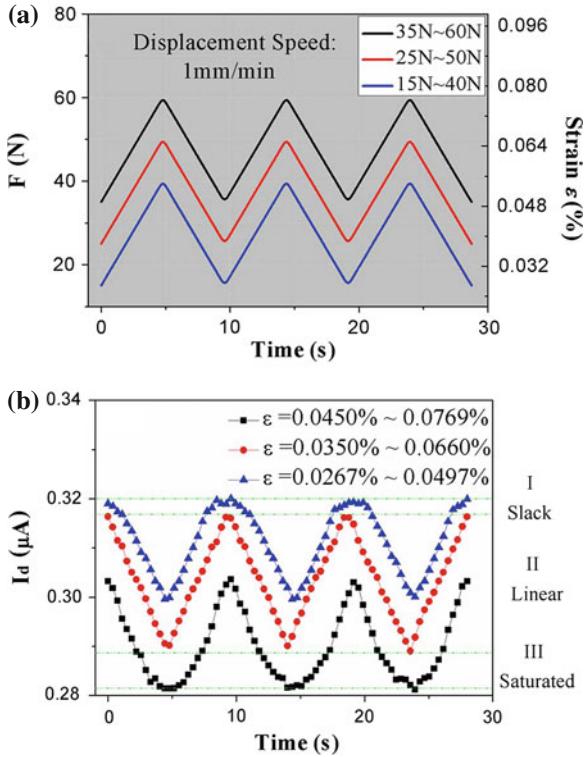


**Fig. 9.5** **a** Measured free end force and strain of the loading machine. **b** Dynamic current response of the suspended SWCNT array strain sensor subjected to three different strain intervals at 0.1 Hz. From Zheng et al. [44]

Aligned CNTs are also used as pressure and flow sensors. The pressure and flow sensing mechanism relies on the negative temperature coefficient of resistance of the CNTs and the thermistor effect of an electrothermally heated CNTs, as well as on the temperature-dependent tunneling rate at the CNT/silicon interface [45]. Figure 9.6a shows a schematic view of a CNT-based pressure and flow sensor and its electrical circuit configuration. The CNTs are grown only on the sidewalls of the silicon microelectrodes, connecting the microelectrodes and substrate that are electrically isolated by a buried oxide layer before the synthesis of the CNTs. A constant bias voltage is applied between the microelectrode and substrate, and the change of current flowing through the CNTs is monitored with respect to the variation of nitrogen pressure and flow velocity. An SEM image of the aligned CNTs are shown in Fig. 9.6b.

The electrical resistance of the sensor decreases linearly as the temperature increases in the range between 298 and 393 K. The temperature of the CNTs depends on the loss of thermal energy due to heat transfer through the surrounding gas mole-

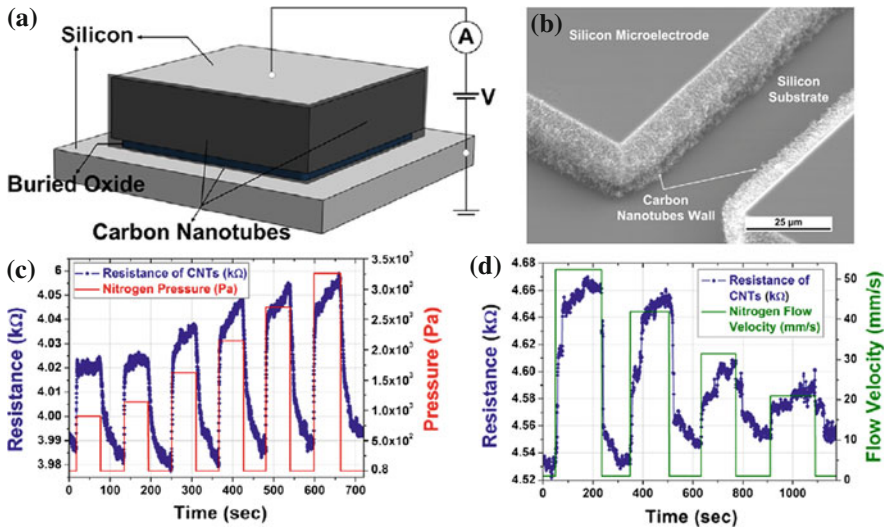


**Fig. 9.6** **a** Schematic structure of a pressure and flow velocity sensor consisted of aligned CNTs based on the electrothermal-thermistor effect. The CNTs are grown on the silicon microelectrode, and the bias voltage and the current are applied and monitored through the CNTs. **b** SEM image of the silicon microelectrode, silicon substrate, and aligned CNTs. **c** Dynamic responses of different nitrogen pressure with a bias of 25 V applied to the sensor. The electric resistance of the sensor increases as the nitrogen pressure is elevated. **d** Nitrogen flow velocity sensing results with 25 V bias voltage. The resistance of the sensor increases with increasing nitrogen flow velocity. From Choi et al. [45]

cules when the supply of constant electrical energy on the CNTs is maintained [45]. Hence, the pressure and flow velocity change induces a temperature change in the CNTs and at the interface between the CNTs and silicon that is monitored by measuring the resistance change.

The responses of the CNT pressure sensor to various nitrogen pressure are presented in Fig. 9.6c. The resistance increases under the elevated pressure and recovered when the pressure is lowered, exhibiting slight signal drift, when the applied bias of 25 V between the microelectrode and substrate is maintained as constant during the experiment. The responsiveness,  $\Delta R/R$ , increases monotonically as a function of pressure increase. The flow velocity sensing capability of the CNTs is also demonstrated in Fig. 9.6d, based on the same mechanism as pressure sensing, wherein the resistance of the CNTs increases with an increase in flow velocity. The resistance of the CNTs immediately increases with respect to an abruptly increased nitrogen flow velocity as the baseline nitrogen flow velocity of 1 mm/s is sequentially modulated to 52.4, 41.9, 31.4 and 20.9 mm/s.

Coated CNT arrays can also be used as flow-rate sensors. Experimental results show that, after a thin  $\text{Al}_2\text{O}_3$  coating on CNTs, the CNT array flow-rate sensor has higher sensitivity and faster response than a conventional platinum hot-wire flow-rate

sensors [46]. Such coated CNT flow-rate sensor has better repeatability than its bare counterpart due to insulation from the surrounding environment.

## 9.2 Electrical Devices

SWCNTs are metallic or semiconducting according to their structures. The electronic properties of perfect MWCNTs are rather similar to those of perfect SWCNTs. In the 1D electronic structure, electrons transport in metallic SWCNTs and MWCNTs over long nanotube lengths, carrying high current densities [47]. Such electrical properties make CNTs having important applications in electronics.

Many researches have been carried out to add random CNTs into various composites to enhance electrical conductivity. Depending on the composite matrix, conductivities of 0.01–10 S/m can be obtained for 5 wt% MWCNT loading or 0.1–0.2 wt% SWCNT loading in polymers. Such CNT composites with high conductivities can dissipate electrostatic charges [48, 49], having potential applications in electrostatic discharge and electromagnetic radio interference protection. The preparation and electrical properties of random CNT composites are reviewed [50] and the readers are referred to the research papers in the review.

The electrical conductivity of CNT composites also depends on the alignment as well as the concentration of CNTs [51, 52]. Here, we review several electrical applications of aligned CNTs without matrices.

### 9.2.1 Random Access Memory

Aligned CNTs can serve as addressable electromechanical switches arrayed across the surface of a microchip, storing hundreds of gigabits of information as random access memory (RAM) (Fig. 9.7). When an electric field is applied to a nanotube, the electric field causes the CNT flex downward into a depression onto the chip surface, where it contacts metal electrodes (in another design, the CNTs touch other nanotubes [54]). The binary 0 state corresponds to the nanotubes suspended and not making contact with the electrode (Fig. 9.7b). When a transistor turns on, the electrode produces an electric field that causes the aligned CNTs to bend and touch an electrode, a configuration that denotes a 1 state (Fig. 9.7c). Van der Waals forces hold the switch in place until application of a field of different polarity causes the nanotubes to return to their straightened positions.

Compared with conventional memories, dynamic random access memory, static random access memory, and flash memory, the CNT-based data storage devices have higher cell density, lower programming voltage, 22 nm process technology while both reading speed and writing speed are fast [53].

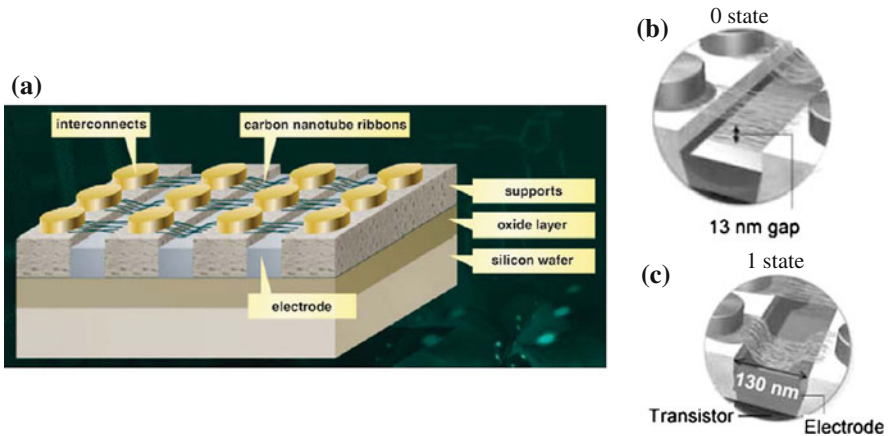


**Fig. 9.7** a RAM made with aligned CNTs. b 0 state. c 1 state. From Bichoutskaia et al. [53]. Copyright (2008), Elsevier

### 9.2.2 Low $\kappa$ Dielectrics

Electrically insulating layers are required in integrated circuits on semiconductor substrates to reduce the coupling capacitance of interconnects. The low  $\kappa$  materials are employed as the insulating layers in integrated circuits to reduce the coupling capacitance. Amorphous silicon dioxide with or without fluorine, hydrogen, or alkyl groups is often used as the dielectric to electrically insulate the metallic interconnects from one another.

The relative dielectric constant of electrically insulating layers can be reduced further by introducing cavities into the low  $\kappa$  materials. The  $\kappa$  value decreases linearly with the cavity volume fraction. The simulation calculations demonstrate that the effective  $\kappa$  value is also affected by the morphology of the cavities. If elongated and oriented pores are used, it is possible to reduce significantly the effective  $\kappa$  value without increasing the proportion of the cavity volume in a dielectric. With the same proportion of cavity volume, a reduction of 13% is achieved with a cavity aspect ratio of 4:1 and a reduction of 20% is achieved with a cavity aspect ratio of 24:1 when the cavities are oriented perpendicularly to an electric field.

CNTs have a high aspect ratio and can be used to introduce elongated, oriented pores into a low  $\kappa$  dielectric to further reduce the effective  $\kappa$  value of the dielectric.

In a typical procedure, aligned CNT forests are grown on a desired surface using PECVD methods as described in Sect. 6.1. Silicon dioxide is deposited between and on top of CNTs. The top oxide is removed by mechanical polishing or by a dry-etch process to expose the CNTs. Then the CNTs are subsequently removed by high-temperature oxidation and/or oxygen or hydrogen plasma.

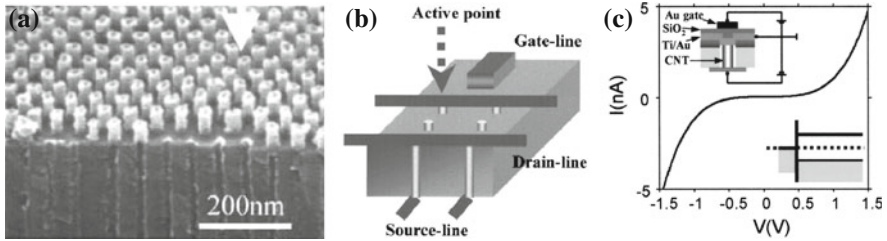


**Fig. 9.8** Architecture of a CNT transistor array. (a) Vertically grown CNTs with diameter of 20 nm and height of 40 nm. (b) Structure of a CNT transistor. (c) Current-voltage diagram of a vertically oriented CNT transistor at a temperature of 4.2 K. No bias is applied to the gate. From Choi et al. [55]. Copyright (2001), American Institute of Physics

### 9.2.3 Transistors

Figure 9.8 shows a transistor array made from vertically aligned CNTs grown on a template of porous aluminum oxide described in Sect. 6.1.6.2. In the integrated device, each CNT is electrically attached to a source electrode (lower electrode in Fig. 9.8b) and a drain electrode (upper electrode in Fig. 9.8b). The gate electrode is located close to the nanotubes. Current flows from the source electrode to the drain electrode and can be switched on or off by applying a voltage to the gate. Figure 9.8c shows a current-voltage curve of the CNT transistor.

Recently, the effects of CNT lengths, CNT diameters, source and drain contacts have been systematically investigated [56].

## 9.3 Acoustic Sensors

### 9.3.1 Artificial Ears

CNT arrays are also used to detect sound as an ear [57]. The CNT arrays bend in response to acoustic energy. The motion of CNTs is transformed to an electrical signal that can be received by a standard electrical sensor. Such sensors can detect much fainter sounds than ears and provide directional information of sounds.

### 9.3.2 Thermoacoustic Loudspeakers

The thermoacoustic phenomenon was discovered in the late nineteenth century. When an alternating current passes through a thin conducting plate or wire, a periodic heating takes place in the conductor because of Joules effect, following the periodic

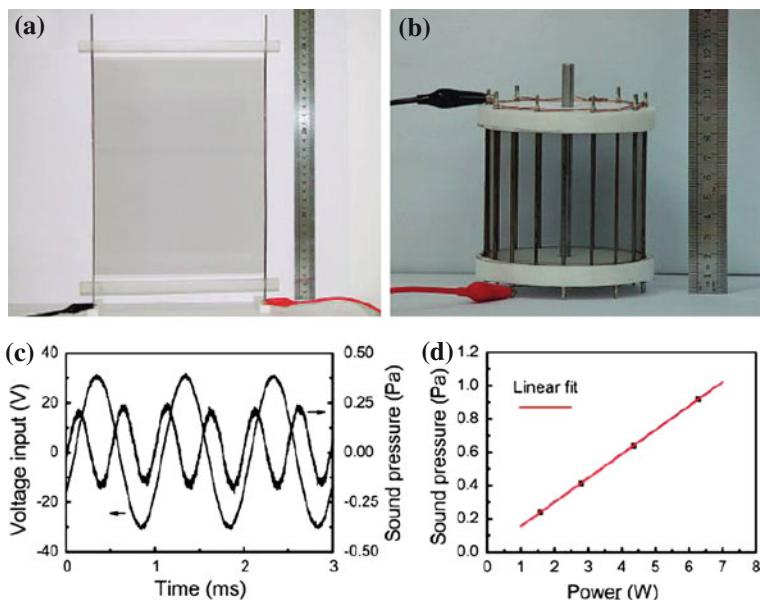


**Fig. 9.9** Thermoacoustic CNT loudspeaker. Optical images of thermoacoustic CNT sheet loudspeakers with **a** planar structure and **b** cage structure. **c** Real-time signals of the input voltage of a CNT thin-film loudspeaker and the output sound pressure. The phase shift between the input voltage and the output sound pressure signal is primarily due to the sound propagation from the CNT sheet to the microphone detector. **d** Sound pressure versus power of CNT thermoacoustic speaker. From Xiao et al. [61]. Copyright (2008) American Chemical Society

change of the current amplitude. This periodic heating causes a periodic temperature oscillation that heats the surrounding medium (usually air) near the conductor surface, resulting in the contraction and expansion of molecules near the conductor while the conductor remains static. The vibrating movement of the molecules results in the generation of an acoustic wave. In a conventional thermoacoustic device (thermophone), the acoustic element is a thin metal film such as a gold film with a thickness of 285 nm [58] and a platinum strip with a thickness of 1.8  $\mu\text{m}$  [59].

To obtain appreciable amplitudes of acoustic waves, it is essential that the conductor be very thin and its heat capacity be very low to conduct the produced heat at a high rate [59]. CNTs have an extremely low heat capacity and good thermal conductivity. CNT sheets can be heated up to 2000  $^{\circ}\text{C}$  in less than 1 ms, and the sheet temperature synchronizes with electrical currents in a wide frequency range of 1–10<sup>5</sup> Hz [60] because of extremely low heat capacity and high thermal conductivity of CNTs. The thickness of present CNT sheets is less than microns. So CNT sheets are one of the best candidates for thermoacoustic devices.

Figure 9.9a, b shows CNT sheet loudspeakers. The CNT sheets are directly drawn out from CNT forests consisting of super aligned CNTs with diameters of 10 nm. The dry-spinning method is described in Sect. 6.2. The thickness of the CNT sheet

is of tens of nanometers. The CNT sheet loudspeaker is formed by directly putting the CNT sheet on two electrodes. When a sinusoidal voltage is applied across the two electrodes, clear and loud tones are emitted from the CNT sheet.

Figure 9.9c shows the input voltage and the output sound pressure. The output sound pressure is measured by a microphone near the CNT sheet. It is noted that the frequency of the sound pressure doubles that of the input voltage, as observed in a conventional thermophone. When an alternating current passes through the CNT sheet, the CNT sheet is heated twice, once during positive and once during negative half-cycles of the alternating current, resulting in a double frequency temperature oscillation, as well as a double frequency sound pressure [61]. The output sound with doubled frequency always sounds strange. In order to reproduce human voice and music with normal frequency without introducing the double frequency effect, a direct current bias must be superimposed to the alternating current. When the strength of the direct current is several times higher than that of the alternating current, the double frequency effect can be negligible [59]. Then the CNT sheet loudspeaker can possess all the functions of a voice-coil loudspeaker [61].

The CNT sheet loudspeaker can generate sound in a wide frequency range 1–10<sup>5</sup> Hz. The high sound pressure level increases with increasing frequency and the sound pressure is proportional to the input power (Fig. 9.9d). The sound pressure produced by the CNT sheet under an alternating current can be expressed as [61]

$$P_{rms} = \left( \frac{\sqrt{\alpha} \rho_0}{2\sqrt{\pi} T_0} \times \frac{\sqrt{f}}{C_s} \right) \frac{P_{input}}{r} \quad (9.2)$$

in an open system (a more accurate while more complex expression is derived in some references [61, 62]), in which  $C_s$  is the heat capacity per unit area of the CNT sheet,  $f$  the frequency of sound,  $P_{input} = I^2 R$  the input electrical power proportional to the square of applied root-mean-square (rms) current  $I = I_0 \sin(\omega t)$ ,  $R$  the resistance of the CNT sheet,  $r$  the distance between the thin CNT sheet conductor and the sound pressure detector (microphone),  $\rho_0$ ,  $T_0$ , and  $\alpha$  the density, average temperature, and thermal diffusivity of the surrounding medium, respectively, and  $P_{rms}$  the rms sound pressure.

Equation 9.2 indicates that the produced sound pressure decreases rapidly with distance. Usually, the temperature of the CNT sheet is a sinusoid of time, and the temperature waves propagate into the atmosphere on either side. The periodic temperature change in the thin boundary layer near the CNT sheets accounts for the sound vibration. Calculation shows that the temperature waves propagate into the working medium and are practically extinguished after one wavelength (27  $\mu\text{m}$  in air and 2.0  $\mu\text{m}$  in water) has been traversed [59].

According to Eq. 9.2, the sound pressure generated by CNT sheet loudspeaker is 260 times higher than that generated by a conventional thermophone with a 700 nm-thick Pt film as the acoustic element, corresponding to a 48 dB difference in the sound pressure level [61]. The measured sound pressure level of the CNT loudspeaker is over 100 dB at high frequencies, higher than the conventional thermoacoustic device with a gold film of 285 nm in thickness as the acoustic element (63 dB) [58].

More detailed works indicate that the heat capacity of the gas also affects the generated sound pressure. Theoretical derivations show that the sound pressure generated by CNT thin films is approximately proportional to the inverse of the heat capacity of the gas within the audible frequency range of human hearing [63].

Besides the freestanding CNT sheet loudspeaker, CNT sheets are also encapsulated into an argon- or air-filled chamber. Such encapsulated CNT loudspeakers can be used in liquids, such as water [64]. In the small enclosure, the sound pressure is

$$P_{\text{rms}} = \frac{\sqrt{\alpha} \rho_0 T_{\text{surf}}^{1/4}}{V_0 T_{\text{ave}} C_s f^{3/2}} \times P_{\text{input}} \quad (9.3)$$

where  $T_{\text{surf}}$  is the temperature of the surface of the CNT sheet,  $T_{\text{ave}}$  the average temperature of the filled gas, and  $V_0$  the volume of the enclosure [59]. The produced pressure causes a vibration of the attached enclosure windows with a resonant frequency  $f_r$  ( $f_r = 3.28 \text{ kHz}$  when working in air and  $1050 \text{ Hz}$  when immersed in water [64]). The highest sound pressure level is over 130 dB, 30 dB higher than that exposed to air.

The pressure generation efficiency coefficient

$$\xi = (\sqrt{\alpha} \rho_0 / 2\sqrt{\pi} T_0) (\sqrt{f} / C_s) \quad (9.4)$$

is affected by many parameters [64], such as (1) the ability of the CNT sheet to be rapidly electrically heated and then to transfer heat to the surrounding medium at high rates, thereby returning to a starting temperature within the excitation cycle; (2) the working medium, which enables rapid heat transfer while minimizing effective increase in the heat capacity of the projector material, and surviving the possible extreme temperature of the CNT sheets; and (3) possible packaging, which provides protection for the CNT sheets and efficient transmission of internal acoustic oscillation to external locations. Theoretical calculation indicates that a CNT sheet working in argon has a higher generation coefficient than that in air or in helium while 100 times higher than that working in liquids, such as water, methanol, and ethanol [64]. The total energy conversion efficiency of the argon-encapsulated thermoacoustic device is 0%, while that of CNT freestanding sheet device in air does not exceed 0.001%.

Additionally, the experimental efficiency of nanoscale thermophones is one order of magnitude below the theoretical expectation [65]. At low frequencies this mainly results from the presence of a substrate. At high frequencies, on the other hand, the efficiency is limited by the heat capacity of the nanowires.

Similar thermoacoustic CNT speakers made of CNT networks are also demonstrated recently [66]. A strong acoustic output was observed in a wide frequency range from 100 Hz to 100 kHz. Sound pressure level measured from 0.5 m away was extremely broad and flat in the ultrasonic region from 40 to 100 kHz.

Based on the same principle, graphene can also be used as speaker to produce sound in the wide ultrasound range 20–50 kHz [67]. The sound pressure depends

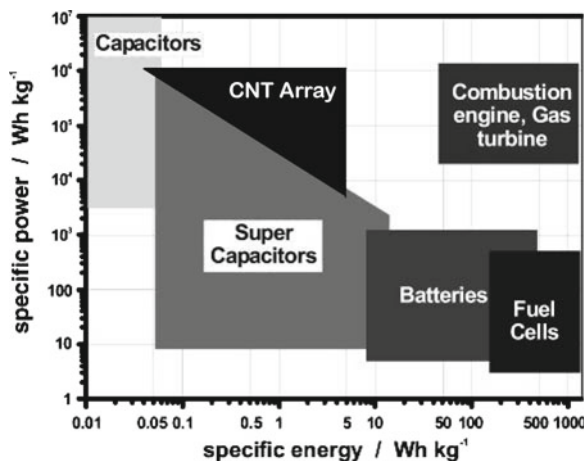


**Fig. 9.10** Simplified Ragone diagram of the energy storage domains for the electrochemical energy conversion systems compared to the internal combustion engine, turbines, and conventional capacitors. From Winter and Brodd [69]. Copyright (2004) American Chemical Society

linearly with frequency of the signal generator from 3 to 20 kHz while independent on the frequency in the ultrasonic region, ranging from 20 to 50 kHz.

Besides the AC electric fields, laser can also generate ultrasound by exploiting the high frequency spectra of laser pulses to achieve broad acoustic bandwidths [68]. Such optoacoustic transmitters made of CNT arrays generate very strong optoacoustic pressure: 18 times stronger than a Cr film reference and five times stronger than a gold nanoparticle composite with the same polymer under pulsed laser excitation. The frequency of the produced strong and high sound covers the DC frequency up to 120 MHz.

## 9.4 Electrochemical and Chemical Storage Devices

Systems for electrochemical energy storage and conversion include batteries, fuel cells, and electrochemical capacitors [69]. Although the mechanisms are different, the common features are that the energy-providing processes take place at the phase boundary of the electrode/electrolyte interface and that electron and ion transports are separated. All of them consist of two electrodes in contact with an electrolyte solution. Figure 9.10 is a simplified Ragone-diagram disclosing the specific power and specific energy of these three electrochemical storage systems. Fuel cells can be considered to be high-energy systems and capacitors to be high-power systems while batteries have intermediate power and energy characteristics. Although no single electrochemical power source can match the characteristics of the internal combustion

engine (high power and high energy), some hybrid electrochemical power sources combining fuel cells (deliver high energy) and capacitors (provide high power) will be competitive with regard to the combustion engines and turbines in the future.

Here, we talk about the applications of CNT arrays in batteries, fuel cells, and capacities as electrodes.

Most favorable electrodes in these electrochemical storage systems are porous electrodes with large surface areas and low polarization. The porous structures of electrodes increase the surface area for reaction and shorten the diffusion path lengths to the reaction sites [69]. The effectiveness of a porous electrode can be estimated from the active surface area and the penetration depth of the reaction process into the porous electrode.

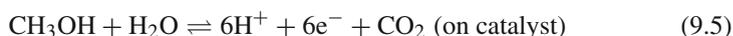
CNTs are the electrode material of choice because a CNT combines a large surface area wetted by an electrolyte, a high electrical conductivity, and a high chemical, mechanical, and electrochemical stability. So the electrochemical behaviors of CNTs have been studied [70–79] because of good electrical conductivity/chemical inertness/wide potential range.

Below, we discuss the application of aligned CNT arrays as porous electrodes in these chemical storage devices. Because of the large electrochemically accessible surface area of CNT arrays, combined with their high electrical conductivity and useful mechanical properties, CNT arrays are attractive as electrodes for devices that use electrochemical double-layer charge injection [48].

### 9.4.1 Fuel Cells

Fuel cells, one kind of electrochemical energy storage devices, are made up of three sandwiched segments similar to ultracapacitors and batteries: an anode, an electrolyte, and a cathode, in a reaction cell. Different from ultracapacitors and batteries in which the energy is stored in the cells and consumed, electricity is produced inside the fuel cells through the reactions between an external fuel and an oxidant in the presence of an electrolyte. At the anode, a catalyst, usually Pt nanoparticles, oxidizes the fuel, usually hydrogen, hydrocarbons, and alcohols, turning the fuel into positively charged ions and negatively charged electrons. The electrolyte (usually composed of aqueous alkaline solution, polymer membrane, phosphoric acid, molten carbonate, and solid oxide substrates) blocks the transportation of electrons while conducting ions. On the cathode, the ions traveling through the electrolyte are reunited with the electrons passing through a load during a reaction with an oxidant, such as oxygen, chlorine, and chlorine dioxide, to produce water or carbon dioxide.

In a typical fuel cell using methanol as the fuel, methanol is oxidized to produce ions and electrons at the anode in a polymer electrolyte:



and oxygen combines with electrons and  $H^+$  ions at the cathode catalyst surface to form water:



Fuel cells can operate continuously as long as the fuels and the oxidants are well maintained [69].

Platinum and platinum alloys seem to be the best choice of catalysts for the electroreduction of oxygen in an acidic media [80]. The catalytic nanoparticles are deposited on porous materials, such as activated carbon, as electrodes. The electrocatalytic activity of platinum catalyst is dependent on many factors [81]. Among them, the good properties of the catalyst supports, such as high surface area and good electrical properties, are essential for a Pt catalyst to highly promote catalytic activities [82].

The large accessible surface area, low resistance, and high stability of CNTs [83, 84] suggest that CNTs are suitable materials for electrodes and catalyst supports in fuel cells. The nanoparticles with electrocatalytic activities may decorate the external walls or be encapsulated in the interior of the CNTs [85]. Several papers have studied the electrocatalytic properties of tangled and substrate-free CNTs [86–91]. More details of electrocatalytic activities using CNT electrodes are reviewed recently [92, 93]. Pt has been deposited on activated SWCNTs or MWCNTs by chemical reduction methods and the resultant electrodes show good electrocatalytic properties for hydrogenation [87], and oxygen reduction [86, 89]. Below we review the electrocatalytic properties of CNT arrays.

Experiments show that no  $O_2$  reduction current is observed using CNT array electrodes or using graphite electrodes over the studied potential range [83]. This means that the CNT arrays and the graphite substrate result in no obvious electrocatalytic activities.

After Pt coating, electrocatalytic activity of CNT is observed. Pt nanoparticles can be deposited on the as-grown CNT arrays by a DC sputtering method [94] or other methods. Figure 9.11 shows the electrocatalytic properties of a Pt/CNT electrode for oxygen reduction reaction investigated by linear sweep voltammetry in a 0.1M  $H_2SO_4$  aqueous solution. The well-aligned CNT arrays are synthesized by the PECVD method (see Chap. 5) on a titanium substrate as the working electrode. The CNT diameters are 50–70 nm and the lengths are 3–4  $\mu m$  [83]. Pt catalysts are deposited on the CNT arrays using a potential-step electrodeposition method.

For Pt/CNT electrodes, a large oxygen reduction current is observed at 0.36 V, which is the typical potential for oxygen electroreduction on platinum catalysts in a  $H_2SO_4$  solution [83]. The specific current, defined by peak current density ( $mA/cm^2$ ) per unit of deposition charge ( $C/cm^2$ ) [83] is used to evaluate the electrocatalytic activity of Pt catalysts for oxygen reduction activities. When the Pt loading mass is low (deposition charge:  $9.744 C/cm^2$ ), the specific current of the Pt/CNT electrode (solid curve in Fig. 9.11a) is  $0.41 mA/\mu C$ , which is 1.4 times as large as that of a Pt/graphite electrode (dashed curve in Fig. 9.11a). At a high deposition charge ( $572.5 \mu C/cm^2$ ), the specific current of the Pt/CNT electrode (solid curve in Fig. 9.11b) is almost twice as large as that of a Pt/graphite electrode (dashed curve

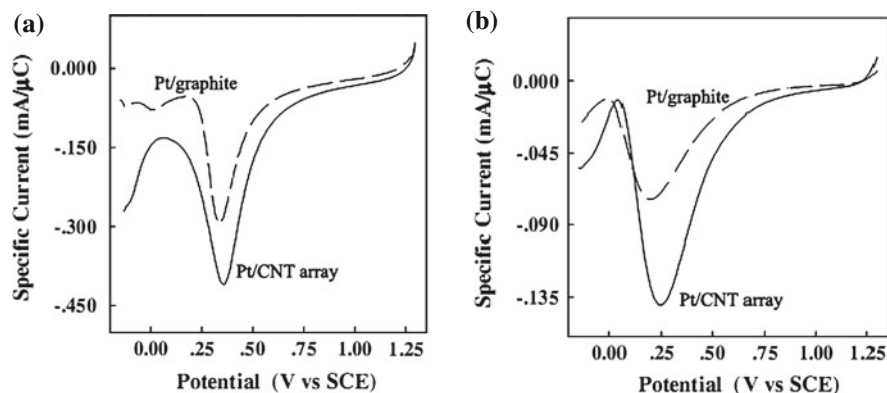


**Fig. 9.11** The linear sweep voltammograms of Pt/CNT arrays in  $N_2$  saturated  $0.1\text{ M H}_2\text{SO}_4$  aqueous solution. For comparison, the voltammograms of platinum-electrodeposited graphite disk electrode (geometry area  $1.71\text{ cm}^2$  prepared at the same conditions) are also plotted as dashed curves. (a) Pt nanoparticles disperse individually on CNT walls with a deposition charge of  $9.744\text{ }\mu\text{C}/\text{cm}^2$ . (b) Pt nanofilm is deposited on individual CNTs with a deposition charge of  $572.5\text{ }\mu\text{C}/\text{cm}^2$  while the coated CNTs huddle together to form bundles of 2–10 CNTs. Linear sweep rate is  $200\text{ mV/s}$ . Pt catalytic nanoparticles are also deposited on a conventional graphite electrode for comparison. From Tang et al. [83]. Reprinted with permission from Elsevier

in Fig. 9.11b). These results imply that the Pt/CNT electrodes possess higher electrocatalytic activities for oxygen reduction.

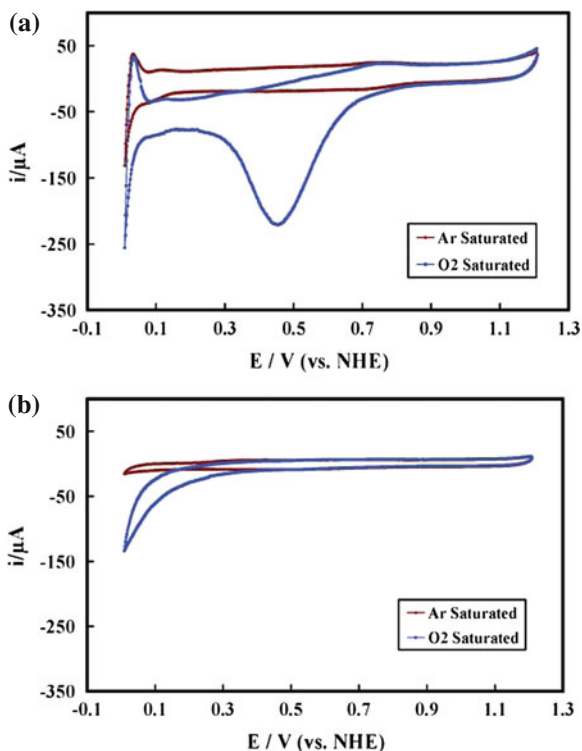
The increase in the  $O_2$  reduction activity of Pt/CNT array electrodes may be attributed to the following two factors: (1) high dispersion of Pt nanoparticles on the 3D structure of CNT electrodes can provide large acceptable surface areas of Pt nanoparticles for oxygen reduction; (2) the particular structure and electrical properties of CNT arrays may be beneficial to the electrocatalytic reduction of oxygen. A previous study on the dissociation of adsorptive oxygen on the surface of CNTs suggested that CNTs have the ability to promote electron-transfer reactions [79]. Additionally, the activity of the catalyst, which could be involved in the interaction between metallic catalyst and catalyst support, can be strongly affected by the properties of the supporting materials. These results imply that well-aligned CNT arrays may be a good candidate for the cathodic catalyst supports in fuel cells.

More detailed studies on the kinetics of oxygen reduction reaction at Pt/CNT electrodes indicated that the activation energy of Pt/CNT electrodes is lower than that of Pt/graphite electrodes at the same cathodic over potential [83]. This suggests that CNTs have a beneficial effect on the kinetics of oxygen reduction.

Pt/CNT arrays can also oxidize methanol [95]. Additionally the oxidation activity of the Pt/CNT electrodes is increased after nitrogen doping.

Besides working as novel catalyst supports (including random CNTs [91, 96] and CNT arrays [83]), CNT arrays with iron catalyst may highly promote electrocatalytic activity themselves after nitrogen doping and can replace Pt catalysts [84, 87, 97, 98]. Figure 9.12 shows the cyclic voltammograms for CNT arrays taken in either argon- or

**Fig. 9.12** Cyclic voltammograms of (a) nitrogen-doped CNT arrays and (b) CNT arrays without nitrogen measured in a 0.6M HCl electrolyte saturated with argon or oxygen at a scan rate of 10 mV/s. Ferrocene is used for CNT catalyst and not removed from CNTs. From Yang et al. [96]. Copyright (2008), The Royal Society of Chemistry



oxygen-saturated aqueous electrolytes. CNT arrays are synthesized using ferrocene as the source of catalyst and ammonia as the nitrogen dopant. The catalytic iron nanoparticles are kept on the CNT tips and the as-synthesized CNT arrays are used as cathodes. The CNTs are doped by nitrogen from ammonia during the CNT growth. The average content of nitrogen of the nitrogen-doped CNT arrays is 3.44 atomic%. Compared with the undoped CNT arrays (Fig. 9.12b), the electrocatalytic activity of the nitrogen-doped CNT arrays is enhanced significantly (Fig. 9.12a), as observed in random CNTs [99]. It is believed that active sites of nitrogen and iron with carbon have contributed to the oxygen reduction reaction.

Recently, it is found that the nitrogen-containing CNT arrays without metal inclusions also promote good electrocatalytic activities. Figure 9.13 plots the cyclic voltammogram for the oxygen reduction reaction of nitrogen-doped CNT array electrodes. The CNT arrays are free of iron catalysts and have a nitrogen content of 4–6 atomic%. Compared to Pt/carbon electrodes, the CNT array electrodes result in a much better electrocatalytic activity, long-term operation stability, and more tolerance to crossover effects than platinum for oxygen reduction in alkaline fuel cells. The vertically aligned CNTs reduce oxygen more effectively in alkaline solutions.

The ends of CNT arrays can be open by femtosecond laser. This Pd-coated end-opened CNT array electrodes perform significantly better than the unprocessed

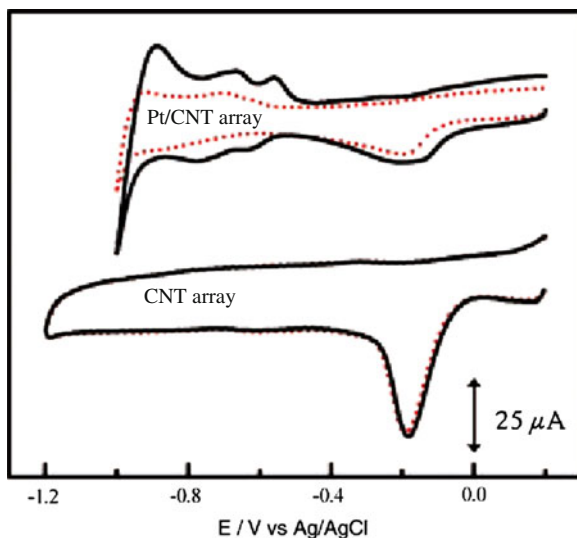


**Fig. 9.13** The cyclic voltammogram for the oxygen reduction reaction of CNT array electrodes before (*solid curves*) and after (*dotted curves*) a continuous potentiodynamic swept for 100,000 cycles in an air-saturated 0.1 M KOH solution at 25 °C. The CNT array electrodes are free of iron catalysts. The properties of Pt/carbon electrodes are also plotted as a reference. From Gong et al. [98]. Copyright (2009), AAAS

Pd-coated CNT array electrodes [100]. Such treated Pd/CNT arrays can oxidate alcohol better in alkaline fuel cells.

### 9.4.2 Supercapacitors

Supercapacitors, also termed as electric double-layer capacitors or ultracapacitors, are electrochemical capacitors that store the electrostatic charges through adsorbing electrolytic ions onto a conductive electrode material with a large accessible specific surface area. The high capacitance of supercapacitors depends on the accessible specific surface area and the double layer adsorbing ions. Supercapacitors can be fully charged or discharged in seconds and achieve a high power output (10 kW/kg) in a few seconds [101] while their energy density ( $\sim 5$  kWh/kg) is lower than that of batteries. Supercapacitors currently bridge the conventional electrolytic capacitors and traditional batteries because they combine the unique properties of conventional capacitors (high power density) and that of traditional batteries (high energy density) [102].

Supercapacitors consist of two electrodes immersed in or impregnated with an electrolyte solution with a semi-permeable membrane serving as a separator that prevents electrical contact between the two electrodes. Figure 9.14 schematically

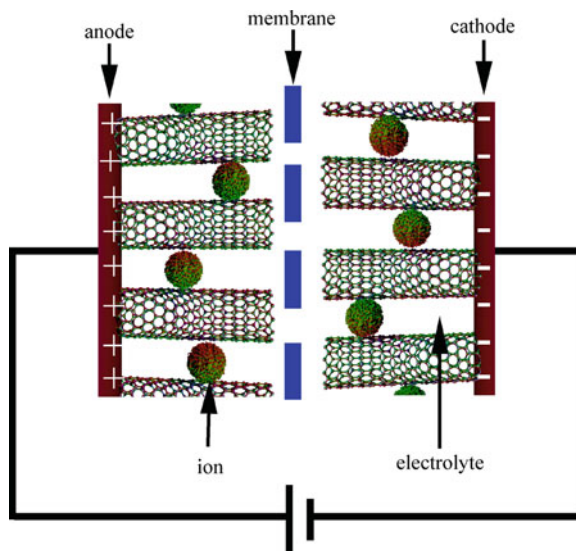


**Fig. 9.14** Schematic of electrochemical double-layer capacitor. The membrane thickness is several nanometers. The potential difference is only several volts

illustrates a supercapacitor made of CNT array electrodes. CNT supercapacitors typically comprise two electrodes separated by an electrically insulating material, which is ionically conducting in electrochemical devices [103, 104]. The capacitance depends on the separation between the charges on the electrodes and the counter-charges in the electrolyte that contributed mostly to the capacitance. Very large capacitances result from the large CNT surface area accessible to the electrolyte.

The CNT array electrodes can be fabricated ex situ or in situ. In ex situ procedures, CNT arrays are grown by CVD methods. Then they are detached from the substrates, re-attached onto an electrically conductive current collector by binding [105], soldering, or surface tension, to form a CNT array electrode. The CNT array electrodes can also be fabricated from random CNTs by self-assembly processes [106]. In in situ procedures, a CNT array can be directly grown on a current collector to form an electrode [107, 108]. The procedure is a one-step process, and the electrical resistance between the CNT array and the current collector is relatively low.

The supercapacitors store the electrostatic charges by reversible absorption of electrolytic ions on active materials with large accessible specific surface areas. When an electric potential is applied to the electrodes, a potential difference is created at the electrode–electrolyte interface because of the charge separation from polarization. This electrostatic interface consists of a double-layer between the ions in the electrolyte and the electrical charges on the electrode.

The capacitance of a supercapacitor is generally assumed to follow that of a parallel-plate capacitor based on the Helmholtz model [109]:

$$C = \frac{\varepsilon_0 \varepsilon_r A}{d} \quad (9.7)$$

where  $\varepsilon_r$  is the dielectric constant of the electrolyte,  $\varepsilon_0$  the permittivity of vacuum,  $A$  the specific surface area of the electrode accessible to the electrolyte ions, and  $d$  the effective thickness of the electrical double layer.

In fact, the structure of the electric double-layer is more complex than the Helmholtz model. The Helmholtz model states that two layers of opposite charges are formed at the electrode–electrolyte interface and are separated by an atomic distance. Besides the Helmholtz model, a modified Gouy-Chapman model refers to a diffuse layer consisting of continuous distribution of electrolyte ions (both cations and anions), not a layer consisting of only cations or only anions, in the electrolyte solution. The modern Stern model combines the Helmholtz model with the Gouy-Chapman model to structure two regions of ion distribution: the inner compact layer (Stern layer) where ions are strongly absorbed by the electrode and an outer diffuse layer defined in the Gouy-Chapman model. The more accurate capacitance is a sum of the capacitances from the two regions:

$$\frac{1}{C} = \frac{1}{C_{\text{Stern}}} + \frac{1}{C_{\text{diff}}} \quad (9.8)$$

Both Stern layer contribution  $C_{\text{Stern}}$  and diffuse layer contribution  $C_{\text{diff}}$  are proportional to the specific surface area and depend on the pore size.

In the supercapacitors, the electrical energy is stored as the electrostatic charges based on the separation of charged species in an electrical double-layer across the electrode-solution interfaces and there is no faradic (redox) reaction.

The active materials with high specific surface area and electrically conducting electron collectors produce high capacitances. In conventional supercapacitors, in which activated carbon or glassy carbon are employed as electrodes, the double-layer capacitance reaches 100–200 F/g in organic electrolytes, and exceeds 370 F/g in aqueous electrolytes [110], storing more energy than the conventional capacitors [111].

CNT arrays store energy by the electrochemical double-layer formed on the surfaces of each CNT in the array. Since the capacitive properties of the array-like CNT membranes were studied [76], capacitance of 18 F/g was obtained in 6 M KOH electrolytes using a 400  $\mu\text{m}$  long CNT array directly grown on a metallic alloy [108], and 35 F/g was obtained in 6 M KOH using a CNT array embedded in cellulose [112].

It is observed that the capacitance of supercapacitors is maximum when the electrode size is close to the ion size [113], confirming the capacitance contribution from pores with sizes smaller than the solvated ion size. CNTs are aligned regularly, possessing regular pore structures, and adjustable pore sizes, and therefore are the best candidates for supercapacitor electrodes. The CNT arrays have larger surface areas than activated carbon to store electron charges in supercapacitors. In addition, the CNT site density can be adjusted to store elementary charges, such as electrons, and consequently the capacitance may be increased considerably.

The capacitances of 180 and 102 F/g are achieved for random SWCNT electrodes and MWCNT electrodes, respectively. It is typically between 15 and 200 F/g when random CNTs are employed [103, 104]. The capacitances come from the large amounts of charge injection when only a few volts are applied.

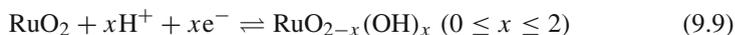
The CNT array electrodes possess lower ion diffusion resistance, higher electrical conductivity, larger pores, and more regular pore structure than the electrodes consisting of random CNTs. Therefore, the CNT array electrodes have higher capacitances, lower resistances, and better rate performances [114]. The application of CNT arrays as capacitors are reviewed recently [102, 110, 114, 115].

Besides aqueous electrolytes, organic electrolytes are also tested. Capacitances of 22 F/g in ionic liquid electrolyte [112], 80 F/g in 1 M tetra-ethylammonium tetrafluoroborate (Et<sub>4</sub>NBF<sub>4</sub>)/propylene carbonate (PC) electrolyte using SWCNT arrays [116], 10–15 F/g in organic electrolytes at an extremely high current density of 200 A/g [117], 83 F/g in organic electrolytes using a DWCNT array of 300 μm in length grown on a conductive Si substrate [118], and 27 F/g in organic electrolytes are reported.

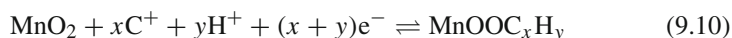
Experimental results indicate that the CNT array electrodes possess lower ion diffusivity resistances and higher electrical conductivities, better rate performances, and higher capacitances than random CNTs because of the regular pore structure and the large pore size of CNT arrays.

Although CNT array electrodes possess a higher rate capability than any other electrochemical electrode materials, their capacitances are moderate, i.e., 10–80 F/g [118, 119], lower than the activated carbon and pseudo-capacitive materials. The moderate capacitance should come from the medium specific surface area of CNTs (120–500 m<sup>2</sup>/g), lower than that of active carbon (1000–3500 m<sup>2</sup>/g) [110]. In order to improve the power and cycle performances of CNT array electrodes, pseudo-capacitive materials (including conducting polymers, such as polyaniline [120], polypyrrole, and polythiophene, metal oxides, such as ruthenium oxide (RuO<sub>2</sub>), manganese oxide (MnO<sub>2</sub>) [121], NiO, Fe<sub>3</sub>O<sub>4</sub>, and nitrides, (such as vanadium nitride) are deposited on the CNT surface to form CNT composite electrodes. In these CNT composite capacitors, CNTs serve as an effective support for pseudo-capacitive materials because of the excellent mechanical properties of CNTs.

At the same time, the CNTs conduct electrons due to superior electrical properties. These pseudocapacitive (or termed redox supercapacitive) materials can be fast and reversible redoxed on the CNT surfaces or near-surface for charge storage and the pseudo-capacitance is faradic. For example, the ruthenium oxidation states in ruthenium oxide can react in electrolyte as [101]



The continuous change of  $x$  during H<sup>+</sup> insertion leads to a pseudo-capacitive behavior with ion adsorption. The charge storage mechanism of manganese oxide is based on the surface absorption of electrolyte cations and proton incorporation:



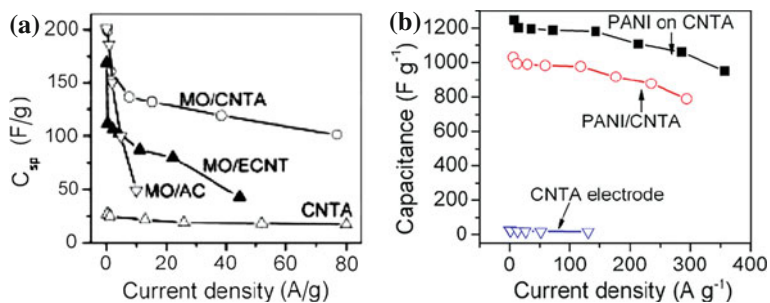


**Fig. 9.15** Specific capacitance of (a) manganese oxide-CNT array (MO/CNTA), manganese oxide-entangled CNT(MO/ECNT), manganese oxide-active carbon (MO/AC), and CNTA versus discharge current density. From Zhang et al. [121]. Copyright (2008) American Chemical Society. (b) Polyaniline (PANI) on CNT array compared with polyaniline/CNTA. From Zhang et al. [120]. Copyright (2008), Elsevier

A study in an electrolyte ionic liquid shows that maximum capacitance is produced when the pore size is close to the ionic radius [113]. So the density of CNT array is usually very high with the gap between CNTs being a few nanometers. So, the conducting polymers and inorganic materials are usually electrodeposited on CNT arrays, like polyaniline (PANI) [120] and  $\text{MnO}_x$  [121].

Such CNT array composites have higher capacitances than CNT arrays and pseudo-capacitive materials due to the contribution of both double-layer capacitance and pseudo-capacitance (Fig. 9.15). The capacitance of the PANI/CNTA composite is 1030 F/g at a low current density of 5.9 A/g [120], higher than the PANI materials. Compared to the best results from commercial products (about 130 F/g), the pseudo-capacitors have much higher energy storage capabilities.

SWCNT arrays are also coated by  $\text{Al}_2\text{O}_3$  to fabricate solid-state dielectric energy storage materials. The solid-state dielectric architecture enables the operation of such devices at substantially higher frequencies than conventional electrolyte-based capacitor designs [122]. Furthermore, modeling of supercapacitor architectures utilizing other dielectric layers suggests the ability to achieve energy densities above 10 Wh/kg while still exhibiting power densities comparable to conventional solid-state capacitor devices.

The SWCNT films were also uniformly spreaded onto the separators serving as both electrodes and charge collectors without metallic current collectors, leading to a simplified and lightweight assembling compact-designed supercapacitor [123]. High energy density of 43.7 Wh/kg and power density of 197.3 kW/kg were achieved from the SWCNT film-based compact-designed supercapacitors with small equivalent series resistance. The specific capacitance of this kind of compact-designed SWCNT film supercapacitor is about 35 F/g.

The advantages of CNT arrays as capacitors come from their excellent mechanical properties, electrical conductivity, and good ion conduction owing to the straight

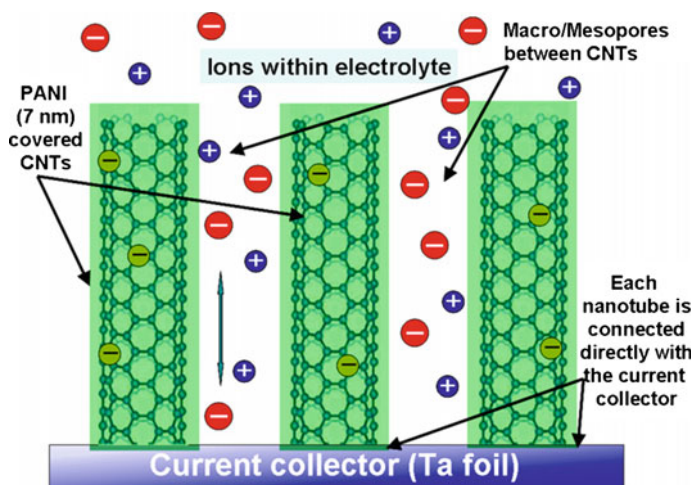


**Fig. 9.16** Schematic diagram showing the Li-ion battery devices with CNT array electrodes as anodes. From Zhang et al. [120]. Copyright (2008), Elsevier

conduction pathways [116]. More detailed applications of CNTs as supercapacitors are reviewed in some literatures [109].

Additionally, the vertical CNT arrays can form effective CNT membranes, which can be electrostatically actuated like the conventional metal plates used in MEMS capacitors [124]. A maximum capacitance of 400 fF and maximum tunability of 5.8% is extracted.

### 9.4.3 Lithium Ion Batteries

In batteries, electrical energy is generated by conversion of chemical energy via a redox reaction at the anode and the cathode in a closed system. Unlike in ultracapacitors where the solvent of the electrolyte is not involved in the charge storage mechanism, the solvent of the electrolyte contributes to the solid-electrolyte interphase in batteries. The Li-ion batteries, one kind of rechargeable batteries, usually consist of an active carbon anode, a lithium-cobalt oxide cathode, and an organic electrolyte.

Activated carbon is used in the commercial lithium-ion batteries as electrodes. In order to obtain better performance of electrodes, CNT arrays and CNT array composites are recently studied as electrodes besides the random CNTs and random CNT composites.

Figure 9.16 illustrates such a Li-ion battery consisting of CNT array (composite) electrodes and a Li electrode. The CNT arrays are prepared by the PECVD method described in Chap. 5. Then a PANI layer is coated on CNTs. Then the PANI/CNT

array composite can be used as the lithium-ion battery cathode [120]. The capacity of such PANI/CNT array composite electrode 98 mAh/g is higher than that of the PANI/random CNT composite electrode 86 mAh/g [125].  $\text{MnO}_x$ /CNT array composite electrodes are also used as cathodes [121]. The capacity of  $\text{MnO}_x$ /CNT array composite (246 mAh/g) is also higher than that of  $\text{MnO}_x$ -based nanostructures. In the CNT array composites, the CNT array framework enhances the rate performance of the electrode materials by providing good electrical conductivity and preserving the benefits of the electrochemical properties of supercapacitive nanomaterials. The CNT array electrodes can also be used as lithium-ion battery anodes [76, 114]. The rate and cycle performance of CNT array electrodes are superior to random CNT electrodes.

#### 9.4.4 Hydrogen Storage

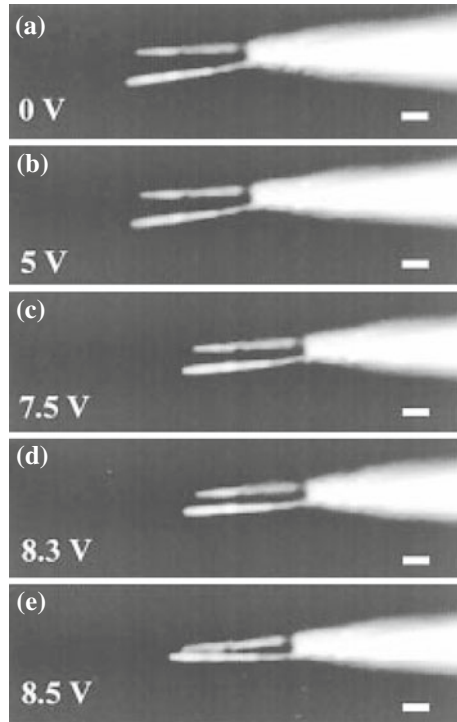
CNTs have been long heralded as potentially useful for hydrogen storage. It was reported that the amount of hydrogen desorbed on SWCNTs is 5–10 wt% at room temperature [126–128], close to the reasonable automotive target of 6.5 wt%. A higher hydrogen storage capacity was also reported in many published papers. For example, it was reported that lithium-doped SWCNTs can absorb 20 wt% of hydrogen at room temperatures under ambient pressures [129]. However, experimental reports of high storage capacities are so controversial [130] that it is impossible to assess the true potential [48]. Careful experiments indicate that the highest absorption percentage of hydrogen is less than 0.1 wt% at room temperature in SWCNTs [131, 132], in MWCNTs [131], and in carbon fibers [133]. More efforts are needed in the field, and the application of CNT arrays in hydrogen storage is still far away from practical applications.

### 9.5 Electromechanical Devices: Actuators

Actuator materials can convert electrical, chemical, thermal, or photonic energies to mechanical energy. Electromechanical actuators are frequently used in robots and typically comprised of two electrodes separated by an electrically insulating material, similar to the supercapacitors. The charge injection causes electrode expansions and contractions that can do mechanical work in the electromechanical actuators [135]. Electrostatic attraction and repulsion between two CNTs were used for cantilever-based nanotweezers [134] (Fig. 9.17) and electromechanically based logic elements [54] and nanoswitches [136].

Macroscaled CNT actuators powered by electricity [135, 137, 138] or fuel [139] can provide a hundred times higher stress generation than natural muscles [140]. The maximum observed isometric actuator stress of SWCNT-sheet actuators is about 26 MPa, 100 times that of the stress generation capability of natural muscles. Aligned

**Fig. 9.17** Electromechanical response of the nanotube nanotweezers. From Kim and Lieber [134]. Scale bar  $1\mu\text{m}$



CNT composites can also be actuators powered by IR irradiation [141] or by electricity [142], and be of shape memory functions [143, 144].

Figure 9.18 shows the CNT aerogel sheets used as the sole component of artificial muscles. The CNT aerogel sheets are fabricated by the spinning method described in Chap. 6. Such muscles can provide giant elongations and elongation rates of 220% and  $3.7 \times 10^4\%$  per second, respectively, at operating temperatures from 80 to 1900K. The width expansion ratio,  $W/W_0$ , increases approximately quadratically with applied voltage  $V$ , while a crossover occurs at higher voltages to a weaker dependence,  $\sim V^{3/2}$ .

## 9.6 Terahertz Sources

CNTs have many properties, from their unique dimensions to an unusual current conduction mechanism, that make them ideal components of electrical circuits. For example, they have shown to exhibit strong electron-phonon resonances. Under certain direct current bias and doping conditions their current and the average electron

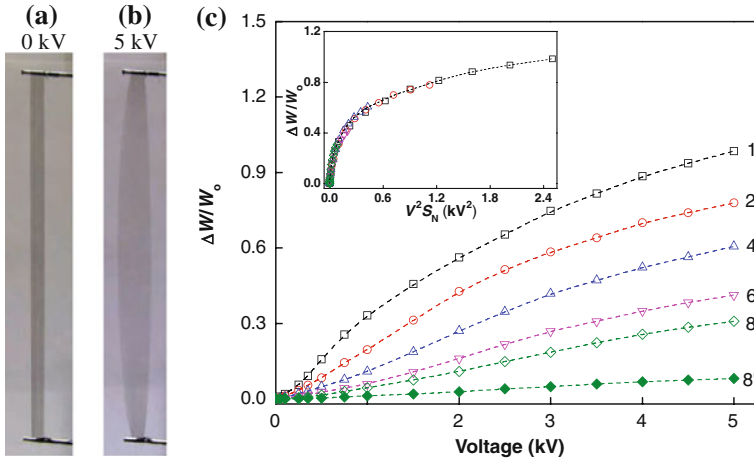


**Fig. 9.18** Artificial muscles. (a) Photograph of a rigidly end-supported nanotube sheet strip with length of 50 mm and width of 2 mm. (b) Same sheet strip expanded in width by applying a 5 kV voltage with respect to ground. (c) Width direction actuation strain,  $W/W_0$  versus applied voltage  $V$  for  $N = 1 - 8$  stacks of single aerogel sheets and for a densified eight-sheet stack, labeled 1 to 8, respectively. From Aliev et al. [145]. Copyright (2009), AAAS

velocity, as well as the electron concentration on the tube, CNTs can oscillate at terahertz frequencies. These resonances could potentially be used to make terahertz sources or sensors.

## 9.7 Other Applications

There are a handful of other applications of assembled CNTs, such as blackbody absorbers to absorb light perfectly across a very wide spectral range (0.2–200  $\mu\text{m}$ ) [147], and infrared (IR) detectors [148, 146] as shown in Fig. 9.19, filters and membranes [149–152], hydrophilicity [153], micro-electro-mechanical-systems [154], gate MOS transistor [155], varactor [156], piezoelectric generators [157], platelet hybrid microstructured reactor [158], ion source in mass spectrometry [159, 160], organic electronic devices [161], microtransducers [162], hazardous industrial chemical gas sensors [163], temperature sensors [164]. As a demonstration, nanotube transistor radios are also fabricated [165], in which SWCNT array devices provide all of the key functions, including resonant antennas, fixed RF amplifiers, RF mixers, and audio amplifiers.

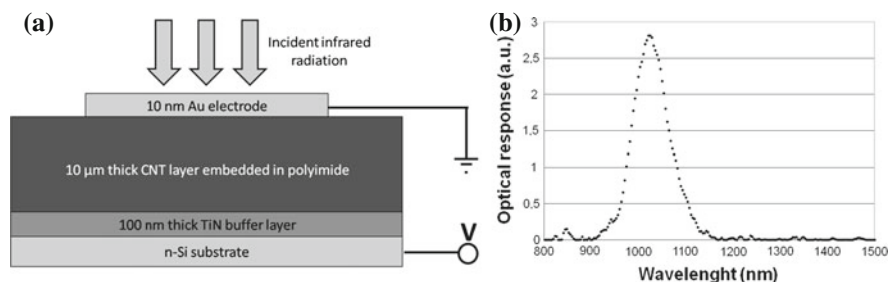


**Fig. 1.19** Infrared sensors. (a) Representation and (b) Spectral response of the CNT IR sensors on silicon (bias voltage of  $-0.18$  V). From Mérel et al. [146]

## References

1. D.A. Walters, L.M. Ericson, M.J. Casavant, J. Liu, D.T. Colbert, K.A. Smith, R.E. Smalley, Elastic strain of freely suspended single-wall carbon nanotube ropes. *Appl. Phys. Lett.* **74**(25), 3803–3805 (1999)
2. M.-F. Yu, B.S. Files, S. Arepalli, R.S. Ruoff, Tensile loading of ropes of single wall carbon nanotubes and their mechanical properties. *Phys. Rev. Lett.* **84**(24), 5552–5555 (2000)
3. A. Krishnan, E. Dujardin, T.W. Ebbesen, P.N. Yianilos, M.M.J. Treacy, Young's modulus of single-walled nanotubes. *Phys. Rev. B* **58**, 14013–14019 (Nov 1998)
4. E.W. Wong, P.E. Sheehan, C.M. Lieber, Nanobeam mechanics: elasticity, strength, and toughness of nanorods and nanotubes. *Science* **277**(5334), 1971–1975 (1997)
5. M.M.J. Treacy, T.W. Ebbesen, J.M. Gibson, Exceptionally high Young's modulus observed for individual carbon nanotubes. *Nature* **381**(6584), 678–680 (1996)
6. M.-F. Yu, O. Lourie, M.J. Dyer, K. Moloni, T.F. Kelly, R.S. Ruoff, Strength and breaking mechanism of multiwalled carbon nanotubes under tensile load. *Science* **287**(5453), 637–640 (2000)
7. C. Wei, K. Cho, D. Srivastava, Tensile strength of carbon nanotubes under realistic temperature and strain rate. *Phys. Rev. B* **67**(11), 115407 (2003)
8. B.M. Nardelli, B.I. Yakobson, J. Bernholc, Mechanism of strain release in carbon nanotubes. *Phys. Rev. B* **57**(8), R4277–R4280 (1998)
9. M. Reibold, P. Paufler, A.A. Levin, W. Kochmann, N. Patzke, D.C. Meyer, Materials: carbon nanotubes in an ancient damascus sabre. *Nature* **444**(7117), 286–286 (2006)
10. K. Sanderson, Sharpest cut from nanotube sword. *Nature* (2006). News at <http://dx.doi.org/10.1038/news061113-11>
11. E.T. Thostenson, W.Z. Li, D.Z. Wang, Z.F. Ren, T.W. Chou, Carbon nanotube/carbon fiber hybrid multiscale composites. *J. Appl. Phys.* **91**(9), 6034–6037 (2002)
12. L. Jin, C. Bower, O. Zhou, Alignment of carbon nanotubes in a polymer matrix by mechanical stretching. *Appl. Phys. Lett.* **73**(9), 1197–1199 (1998)
13. R. Hagenmueller, H.H. Gommans, A.G. Rinzler, J.E. Fischer, K.I. Winey, Aligned single-wall carbon nanotubes in composites by melt processing methods. *Chem. Phys. Lett.* **330**(3–4), 219–225 (2000)
14. B. Safadi, R. Andrews, E.A. Grulke, Multiwalled carbon nanotube polymer composites: synthesis and characterization of thin films. *J. Appl. Polym. Sci.* **84**(14), 2660–2669 (2002)
15. A.R. Bhattacharyya, T. Sreekumar, T. Liu, S. Kumar, L.M. Ericson, R.H. Hauge, R.E. Smalley, Crystallization and orientation studies in polypropylene/single wall carbon nanotube composite. *Polymer* **44**(8), 2373–2377 (2003)

16. E.S. Choi, J.S. Brooks, D.L. Eaton, M.S. Al-Haik, M.Y. Hussaini, H. Garmestani, D. Li, K. Dahmen, Enhancement of thermal and electrical properties of carbon nanotube polymer composites by magnetic field processing. *J. Appl. Phys.* **94**(9), 6034–6039 (2003)
17. X. Zhang, Q. Li, T.G. Holesinger, P.N. Arendt, J. Huang, P.D. Kirven, T.G. Clapp, R.F. DePaula, X. Liao, Y. Zhao, L. Zheng, D. Peterson, Y. Zhu, Ultrastrong, stiff, and lightweight carbon-nanotube fibers. *Adv. Mater.* **19**(23), 4198–4201 (2007)
18. Y. Dror, W. Salalha, R.L. Khalfin, Y. Cohen, A.L. Yarin, E. Zussman, Carbon nanotubes embedded in oriented polymer nanofibers by electrospinning. *Langmuir* **19**(17), 7012–7020 (2003)
19. R. Sen, B. Zhao, D. Perea, M.E. Itkis, H. Hu, J. Love, E. Bekyarova, R.C. Haddon, Preparation of single-walled carbon nanotube reinforced polystyrene and polyurethane nanofibers and membranes by electrospinning. *Nano Lett.* **4**(3), 459–464 (2004)
20. J. Gao, A. Yu, M.E. Itkis, E. Bekyarova, B. Zhao, S. Niyogi, R.C. Haddon, Large-scale fabrication of aligned single-walled carbon nanotube array and hierarchical single-walled carbon nanotube assembly. *J. Am. Chem. Soc.* **126**(51), 16698–16699 (2004)
21. J.J. Ge, H. Hou, Q. Li, M.J. Graham, A. Greiner, D.H. Reneker, F.W. Harris, S.Z.D. Cheng, Assembly of well-aligned multiwalled carbon nanotubes in confined polyacrylonitrile environments: electrospun composite nanofiber sheets. *J. Am. Chem. Soc.* **126**(48), 15754–15761 (2004)
22. M.D. Lynch, D.L. Patrick, Organizing carbon nanotubes with liquid crystals. *Nano Lett.* **2**(11), 1197–1201 (2002)
23. X.L. Xie, Y.W. Mai, X.P. Zhou, Dispersion and alignment of carbon nanotubes in polymer matrix: a review. *Mat. Sci. Eng. R-Rep.* **49**(4), 89–112 (2005)
24. M. Zhang, K.R. Atkinson, R.H. Baughman, Multifunctional carbon nanotube yarns by downsizing an ancient technology. *Science* **306**(5700), 1358–1361 (2004)
25. M.B. Bazbouz, G.K. Stylios, Novel mechanism for spinning continuous twisted composite nanofiber yarns. *Eur. Polym. J.* **44**(1), 1–12 (2008)
26. K. Jiang, Q. Li, S. Fan, Nanotechnology: spinning continuous carbon nanotube yarns. *Nature* **419**(6909), 801–801 (2002)
27. Y.-L. Li, I.A. Kinloch, A.H. Windle, Direct spinning of carbon nanotube fibers from chemical vapor deposition synthesis. *Science* **304**(5668), 276–278 (2004)
28. F. Ko, Y. Gogotsi, A. Ali, N. Naguib, H. Ye, G. Yang, C. Li, P. Willis, Electrospinning of continuous carbon nanotube-filled nanofiber yarns. *Adv. Mater.* **15**(14), 1161–1165 (2003)
29. R.B. Pipes, P. Hubert, Helical carbon nanotube arrays: mechanical properties. *Compos. Sci. Technol.* **62**(3), 419–428 (2002)
30. J.W.S. Hearle, P. Grosberg, S. Backer, *Structural Mechanics of Fibers, Yarns, and Fabrics* (Wiley-Interscience, New York, 1969)
31. J.-P. Salvetat, G.A.D. Briggs, J.-M. Bonard, R.R. Bacsá, A.J. Kulik, T. Stöckli, N.A. Burnham, L. Forró, Elastic and shear moduli of single-walled carbon nanotube ropes. *Phys. Rev. Lett.* **82**, 944–947 (Feb 1999)
32. R.B. Pipes, P. Hubert, Scale effects in carbon nanostructures: self-similar analysis. *Nano Lett.* **3**(2), 239–243 (2003)
33. B. Vigolo, A. Pénicaud, C. Coulon, C. Sauder, R. Pailler, C. Journet, P. Bernier, P. Poulin, Macroscopic fibers and ribbons of oriented carbon nanotubes. *Science* **290**(5495), 1331–1334 (2000)
34. K. Koziol, J. Vilatela, A. Moisala, M. Motta, P. Cunniff, M. Sennett, A. Windle, High-performance carbon nanotube fiber. *Science* **318**(5858), 1892–1895 (2007)
35. S. Kumar, T.D. Dang, F.E. Arnold, A.R. Bhattacharyya, B.G. Min, X. Zhang, R.A. Vaia, C. Park, W.W. Adams, R.H. Hauge, R.E. Smalley, S. Ramesh, P.A. Willis, Synthesis, structure, and properties of PBO/SWNT composites. *Macromolecules* **35**(24), 9039–9043 (2002)
36. L.-Q. Liu, M. Eder, I. Burgert, D. Tasis, M. Prato, H.D. Wagner, One-step electrospun nanofiber-based composite ropes. *Appl. Phys. Lett.*, **90**(8), 083108 (2007)
37. J. Jia, J. Zhao, G. Xu, J. Di, Z. Yong, Y. Tao, C. Fang, Z. Zhang, X. Zhang, L. Zheng, Q. Li, A comparison of the mechanical properties of fibers spun from different carbon nanotubes. *Carbon* **49**(4), 1333–1339 (2011)

38. K. Liu, Y. Sun, L. Chen, C. Feng, X. Feng, K. Jiang, Y. Zhao, S. Fan, Controlled growth of super-aligned carbon nanotube arrays for spinning continuous unidirectional sheets with tunable physical properties. *Nano Lett.* **8**(2), 700–705 (2008)
39. L.M. Ericson, H. Fan, H. Peng, V.A. Davis, W. Zhou, J. Sulpizio, Y. Wang, R. Booker, J. Vavro, C. Guthy, A.N.G. Parra-Vasquez, M.J. Kim, S. Ramesh, R.K. Saini, C. Kittrell, G. Lavin, H. Schmidt, W.W. Adams, W.E. Billups, M. Pasquali, W.-F. Hwang, R.H. Hauge, J.E. Fischer, R.E. Smalley, Macroscopic, neat, single-walled carbon nanotube fibers. *Science* **305**(5689), 1447–1450 (2004)
40. Z. Wu, Z. Chen, X. Du, J.M. Logan, J. Sippel, M. Nikolou, K. Kamaras, J.R. Reynolds, D.B. Tanner, A.F. Hebard, A.G. Rinzler, Transparent, conductive carbon nanotube films. *Science* **305**(5688), 1273–1276 (2004)
41. L. Zhang, C. Feng, Z. Chen, L. Liu, K. Jiang, Q. Li, S. Fan, Superaligned carbon nanotube grid for high resolution transmission electron microscopy of nanomaterials. *Nano Lett.* **8**(8), 2564–2569 (2008)
42. L. Ge, S. Sethi, L. Ci, P.M. Ajayan, A. Dhinojwala, Carbon nanotube-based synthetic gecko tapes. *Proc. Natl. Acad. Sci. U S A* **104**(26), 10792–10795 (2007)
43. N.M. Mohamed, L.M. Kou, Piezoresistive effect of aligned multiwalled carbon nanotubes array. *J. Appl. Sci.* **11**(8), 1386–1390 (2011)
44. F.-Z. Zheng, Z.-Y. Zhou, X. Yang, Y.-K. Tang, Y. Wu, Investigation on strain-sensing suspended single-walled carbon nanotube arrays. *IEEE Trans. Nanotechnol.* **10**(4), 694–698 (2011)
45. J. Choi, J. Kim, Batch-processed carbon nanotube wall as pressure and flow sensor. *Nanotechnology* **21**(10), 105502 (2010)
46. X. Yang, Z. Zhou, D. Wang, X. Liu, High sensitivity carbon nanotubes flow-rate sensors and their performance improvement by coating. *Sensors* **10**(5), 4898–4906 (2010)
47. S. Frank, P. Poncharal, Z.L. Wang, W.A. de Heer, Carbon nanotube quantum resistors. *Science* **280**(5370), 1744–1746 (1998)
48. R.H. Baughman, A.A. Zakhidov, W.A. de Heer, Carbon nanotubes—the route toward applications. *Science* **297**(5582), 787–792 (2002)
49. M.J. Biercuk, M.C. Llaguno, M. Radosavljevic, J.K. Hyun, A.T. Johnson, J.E. Fischer, Carbon nanotube composites for thermal management. *Appl. Phys. Lett.* **80**(15), 2767–2769 (2002)
50. W. Bauhofer, J.Z. Kovacs, A review and analysis of electrical percolation in carbon nanotube polymer composites. *Compos. Sci. Technol.* **69**(10), 1486–1498 (2009)
51. F. Du, J.E. Fischer, K.I. Winey, Effect of nanotube alignment on percolation conductivity in carbon nanotube/polymer composites. *Phys. Rev. B* **72**(12), 121404 (2005)
52. J. Sandler, J. Kirk, I. Kinloch, M. Shaffer, A. Windle, Ultra-low electrical percolation threshold in carbon-nanotube-epoxy composites. *Polymer* **44**(19), 5893–5899 (2003)
53. E. Bichoutskaia, A.M. Popov, Y.E. Lozovik, Nanotube-based data storage devices. *Mater. Today* **11**(6), 38–43 (2008)
54. T. Rueckes, K. Kim, E. Joselevich, G.Y. Tseng, C.-L. Cheung, C.M. Lieber, Carbon nanotube-based nonvolatile random access memory for molecular computing. *Science* **289**(5476), 94–97 (2000)
55. W.B. Choi, J.U. Chu, K.S. Jeong, E.J. Bae, J.-W. Lee, J.-J. Kim, J.-O. Lee, Ultrahigh-density nanotransistors by using selectively grown vertical carbon nanotubes. *Appl. Phys. Lett.* **79**(22), 3696–3698 (2001)
56. X. Ho, L. Ye, S.V. Rotkin, Q. Cao, S. Unarunotai, S. Salamat, M.A. Alam, J.A. Rogers, Scaling properties in transistors that use aligned arrays of single-walled carbon nanotubes. *Nano Lett.* **10**(2), 499–503 (2010)
57. F. Noca, J. Xu, P. Koumoutsakos, T. Werder, J. Walther, in *Nanoscale ears based on artificial stereocilia*, in *The 140th Meeting of the Acoustical Society of America/NOISE-CON*, Newport Beach, California (2000)
58. R.R. Bouillosa, A.O. Santillá, A note on the use of novel thermoacoustic radiators for ultrasonic experiments: the importance of phase in a focused field. *Eur. J. Phys.* **27**(1), 95 (2006)

59. H.D. Arnold, I.B. Crandall, The thermophone as a precision source of sound. *Phys. Rev.* **10**(1) 22–38 (1917)
60. P. Liu, L. Liu, Y. Wei, K. Liu, Z. Chen, K. Jiang, Q. Li, S. Fan, Fast high-temperature response of carbon nanotube film and its application as an incandescent display. *Adv. Mater.* **21**(35), 3563–3566 (2009)
61. L. Xiao, Z. Chen, C. Feng, L. Liu, Z.-Q. Bai, Y. Wang, L. Qian, Y. Zhang, Q. Li, K. Jiang, S. Fan, Flexible, stretchable, transparent carbon nanotube thin film loudspeakers. *Nano Lett.* **8**(12), 4539–4545 (2008)
62. E.C. Wentz, The thermophone. *Phys. Rev.* **19**(4), 333–345 (1922)
63. L. Xiao, P. Liu, L. Liu, Q. Li, Z. Feng, S. Fan, K. Jiang, High frequency response of carbon nanotube thin film speaker in gases. *J. Appl. Phys.* **110**(8), 084311 (2011)
64. A.E. Aliev, M.D. Lima, S. Fang, R.H. Baughman, Underwater sound generation using carbon nanotube projectors. *Nano Lett.* **10**(7), 2374–2380 (2010)
65. V. Vesterinen, A.O. Niskanen, J. Hassel, P. Helistö, Fundamental efficiency of nanothermophones: modeling and experiments. *Nano Lett.* **10**, 5020–5024 (2010)
66. K. Suzuki, S. Sakakibara, M. Okada, Y. Neo, H. Mimura, Y. Inoue, T. Murata, Study of carbon-nanotube web thermoacoustic loud speakers. *Jpn. J. Appl. Phys.* **50**(1), 01BJ10 (2011)
67. H. Tian, T.-L. Ren, D. Xie, Y.-F. Wang, C.-J. Zhou, T.-T. Feng, D. Fu, Y. Yang, P.-G. Peng, L.-G. Wang, L.-T. Liu, Graphene-on-paper sound source devices. *ACS Nano* **5**(6), 4878–4885 (2011)
68. H.W. Baac, J.G. Ok, H.J. Park, T. Ling, S.-L. Chen, A.J. Hart, L.J. Guo, Carbon nanotube composite optoacoustic transmitters for strong and high frequency ultrasound generation. *Appl. Phys. Lett.* **97**(23), 234104 (2010)
69. M. Winter, R.J. Brodd, What are batteries, fuel cells, and supercapacitors? *Chem. Rev.* **104**(10), 4245–4270 (2004)
70. J. Li, A. Cassell, L. Delzeit, J. Han, M. Meyyappan, Novel three-dimensional electrodes: electrochemical properties of carbon nanotube ensembles. *J. Phys. Chem. B* **106**(36), 9299–9305 (2002)
71. J.K. Campbell, L. Sun, R.M. Crooks, Electrochemistry using single carbon nanotubes. *J. Am. Chem. Soc.* **121**(15), 3779–3780 (1999)
72. P. Britto, K. Santhanam, P. Ajayan, Carbon nanotube electrode for oxidation of dopamine. *Bioelectrochem. Bioenerg.* **41**(1), 121–125 (1996)
73. J.M. Nugent, K.S.V. Santhanam, A. Rubio, P.M. Ajayan, Fast electron transfer kinetics on multiwalled carbon nanotube microbundle electrodes. *Nano Lett.* **1**(2), 87–91 (2001)
74. J. Wang, M. Musameh, Y. Lin, Solubilization of carbon nanotubes by Nafion toward the preparation of amperometric biosensors. *J. Am. Chem. Soc.* **125**(9), 2408–2409 (2003)
75. H. Luo, Z. Shi, N. Li, Z. Gu, Q. Zhuang, Investigation of the electrochemical and electrocatalytic behavior of single-wall carbon nanotube film on a glassy carbon electrode. *Anal. Chem.* **73**(5), 915–920 (2001)
76. G. Che, B.B. Lakshmi, E.R. Fisher, C.R. Martin, Carbon nanotubule membranes for electrochemical energy storage and production. *Nature* **393**(6683), 346–349 (1998)
77. M. Musameh, J. Wang, A. Merkoci, Y. Lin, Low-potential stable nadh detection at carbon-nanotube-modified glassy carbon electrodes. *Electrochem. Commun.* **4**(10), 743–746 (2002)
78. Y. Lin, S. Taylor, H.P. Li, K.A.S. Fernando, L.W. Qu, W. Wang, L.R. Gu, B. Zhou, Y.P. Sun, Advances toward bioapplications of carbon nanotubes. *J. Mater. Chem.* **14**(4), 527–541 (2004)
79. P. J. Britto, K.S.V. Santhanam, A. Rubio, J.A. Alonso, P.M. Ajayan, Improved charge transfer at carbon nanotube electrodes. *Adv. Mater.* **11**(2), 154–157 (1999)
80. B.D. McNicol, D.A.J. Rand, K.R. Williams, Direct methanol-air fuel cells for road transportation. *J. Power Sources* **83**(1–2), 15–31 (1999)
81. A. Gamez, D. Richard, P. Gallezot, F. Gloaguen, R. Faure, R. Durand, Oxygen reduction on well-defined platinum nanoparticles inside recast ionomer. *Electrochim. Acta.* **41**(2), 307–314 (1996)

82. J.-S. Yu, S. Kang, S.B. Yoon, G. Chai, Fabrication of ordered uniform porous carbon networks and their application to a catalyst supporter. *J. Am. Chem. Soc.* **124**, 9382–9383 (2002)
83. H. Tang, J.H. Chen, Z.P. Huang, D.Z. Wang, Z.F. Ren, L.H. Nie, Y.F. Kuang, S.Z. Yao, High dispersion and electrocatalytic properties of platinum on well-aligned carbon nanotube arrays. *Carbon* **42**(1), 191–197 (2004)
84. H. Dai, E.W. Wong, C.M. Lieber, Probing electrical transport in nanomaterials: conductivity of individual carbon nanotubes. *Science* **272**(5261), 523–526 (1996)
85. T.W. Ebbesen, P.M. Ajayan, Large-scale synthesis of carbon nanotubes. *Nature* **358**(6383), 220–222 (1992)
86. W. Li, C. Liang, J. Qiu, W. Zhou, H. Han, Z. Wei, G. Sun, Q. Xin, Carbon nanotubes as support for cathode catalyst of a direct methanol fuel cell. *Carbon* **40**(5), 791–794 (2002)
87. V. Lordi, N. Yao, J. Wei, Method for supporting platinum on single-walled carbon nanotubes for a selective hydrogenation catalyst. *Chem. Mater.* **13**, 733–737 (2001)
88. N. Jha, A.L.M. Reddy, M. Shaijumon, N. Rajalakshmi, S. Ramaprabhu, Pt-Ru/multi-walled carbon nanotubes as electrocatalysts for direct methanol fuel cell. *Int. J. Hydrogen Energy* **33**(1), 427–433 (2008)
89. Z. Liu, X. Lin, J.Y. Lee, W. Zhang, M. Han, L.M. Gan, Preparation and characterization of platinum-based electrocatalysts on multiwalled carbon nanotubes for proton exchange membrane fuel cells. *Langmuir* **18**(10), 4054–4060 (2002)
90. R. Yu, L. Chen, Q. Liu, J. Lin, K.-L. Tan, S.C. Ng, H.S.O. Chan, G.-Q. Xu, T.S.A. Hor, Platinum deposition on carbon nanotubes via chemical modification. *Chem. Mater.* **10**, 718–722 (Mar. 1998)
91. J.M. Planeix, N. Coustel, B. Coq, V. Brotons, P.S. Kumbhar, R. Dutartre, P. Geneste, P. Bernier, P.M. Ajayan, Application of carbon nanotubes as supports in heterogeneous catalysis. *J. Am. Chem. Soc.* **116**, 7935–7936 (1994)
92. I. Dumitrescu, P.R. Unwin, J.V. Macpherson, Electrochemistry at carbon nanotubes: perspective and issues. *Chem. Commun.* **2009**(45), 6886–6901 (2009)
93. J.J. Gooding, Nanostructuring electrodes with carbon nanotubes: a review on electrochemistry and applications for sensing. *Electrochim. Acta* **50**(15), 3049–3060 (2005)
94. N. Soin, S. Roy, L. Karlsson, J. McLaughlin, Sputter deposition of highly dispersed platinum nanoparticles on carbon nanotube arrays for fuel cell electrode material. *Diamond Relat. Mater.* **19**(5–6), 595–598 (2010)
95. W.-C. Fang, High methanol oxidation activity of well-dispersed Pt nanoparticles on carbon nanotubes using nitrogen doping. *Nanoscale Res. Lett.* **5**(1), 68–73 (2010)
96. J. Yang, D.-J. Liu, N.N. Kariuki, L.X. Chen, Aligned carbon nanotubes with built-in FeN<sub>4</sub> active sites for electrocatalytic reduction of oxygen. *Chem. Commun.* **2008**(3), 329–331 (2008)
97. H.B. Zhang, X.L. Liang, X. Dong, H.Y. Li, G.D. Lin, Multi-walled carbon nanotubes as a novel promoter of catalysts for CO/CO<sub>2</sub> hydrogenation to alcohols. *Catal. Surv. Asia* **13**(1), 41–58 (2009)
98. K. Gong, F. Du, Z. Xia, M. Durstock, L. Dai, Nitrogen-doped carbon nanotube arrays with high electrocatalytic activity for oxygen reduction. *Science* **323**(5915), 760–764 (2009)
99. P. Matter, U. Ozkan, Non-metal catalysts for dioxygen reduction in an acidic electrolyte. *Catal. Lett.* **109**(3), 115–123 (2006)
100. F. Hu, W. Chen, End-opened carbon nanotube array supported Pd as anode for alkaline fuel cells. *Electrochem. Commun.* **13**(9), 955–958 (2011)
101. B. Conway, *Electrochemical Supercapacitors: Scientific Fundamentals and Technological Applications* (Kluwer, Boston, 1999)
102. J.M. Boyea, R.E. Camacho, S.P. Turano, W.J. Ready, Carbon nanotube-based supercapacitors: technologies and markets. *Nanotechnol. Law Bus.* **4**(1), 585–593 (2007)
103. C. Niu, E.K. Sichel, R. Hoch, D. Moy, H. Tennent, High power electrochemical capacitors based on carbon nanotube electrodes. *Appl. Phys. Lett.* **70**(11), 1480–1482 (1997)
104. K.H. An, W.S. Kim, Y.S. Park, J.-M. Moon, D.J. Bae, S.C. Lim, Y.S. Lee, Y.H. Lee, Electrochemical properties of high-power supercapacitors using single-walled carbon nanotube electrodes. *Adv. Funct. Mater.* **11**(5), 387–392 (2001)

105. H. Zhang, G.P. Cao, Y.S. Yang, Using a cut-paste method to prepare a carbon nanotube fur electrode. *Nanotechnology* **18**(19), 195607 (2007)
106. D. Nkosi, K.I. Ozoemena, Self-assembled nano-arrays of single-walled carbon nanotube-octa(hydroxyethylthio)phthalocyaninatoiron(II) on gold surfaces: impacts of SWCNT and solution pH on electron transfer kinetics. *Electrochim. Acta* **53**(6), 2782–2793 (2008)
107. T. Hiraoka, T. Yamada, K. Hata, D.N. Futaba, H. Kurachi, S. Uemura, M. Yumura, S. Iijima, Synthesis of single- and double-walled carbon nanotube forests on conducting metal foils. *J. Am. Chem. Soc.* **128**(41), 13338–13339 (2006)
108. S. Talapatra, S. Kar, S.K. Pal, R. Vajtai, L. Ci, P. Victor, M.M. Shaijumon, S. Kaur, O. Nalamasu, M.P. Ajayan, Direct growth of aligned carbon nanotubes on bulk metals. *Nat. Nanotechnol.* **1**(2), 112–116 (2006)
109. E. Frackowiak, Carbon materials for supercapacitor application. *Phys. Chem. Chem. Phys.* **9**, 1774–1785 (2007)
110. L.L. Zhang, X.S. Zhao, Carbon-based materials as supercapacitor electrodes. *Chem. Soc. Rev.* **38**(9), 2520–2531 (2009)
111. E. Raymundo-Piñero, K. Kierzek, J. Machnikowski, F. Béguin, Relationship between the nanoporous texture of activated carbons and their capacitance properties in different electrolytes. *Carbon* **44**(12), 2498–2507 (2006)
112. V.L. Pushparaj, M.M. Shaijumon, A. Kumar, S. Murugesan, L. Ci, R. Vajtai, R.J. Linhardt, O. Nalamasu, P.M. Ajayan, Flexible energy storage devices based on nanocomposite paper. *Proc. Natl. Acad. Sci. U S A* **104**(34), 13574–13577 (2007)
113. C. Largeot, C. Portet, J. Chmiola, P.-L. Taberna, Y. Gogotsi, P. Simon, Relation between the ion size and pore size for an electric double-layer capacitor. *J. Am. Chem. Soc.* **130**(9), 730–2731 (2008)
114. H. Zhang, G.P. Cao, Y.S. Yang, Carbon nanotube arrays and their composites for electrochemical capacitors and lithium-ion batteries. *Energy Environ. Sci.* **2**(9), 932–943 (2009)
115. P. Simon, Y. Gogotsi, Materials for electrochemical capacitors. *Nat. Mater.* **7**, 845–854 (2008)
116. D.N. Futaba, K. Hata, T. Yamada, T. Hiraoka, Y. Hayamizu, Y. Kakudate, O. Tanaike, H. Hatori, M. Yumura, S. Iijima, Shape-engineerable and highly densely packed single-walled carbon nanotubes and their application as super-capacitor electrodes. *Nat. Mater.* **5**, 987–994 (2006)
117. Y. Honda, T. Haramoto, M. Takeshige, H. Shiozaki, T. Kitamura, M. Ishikawa, Aligned mwcnt sheet electrodes prepared by transfer methodology providing high-power capacitor performance. *Electrochem. Solid-State Lett.* **10**(4), A106–A110 (2007)
118. T. Iwasaki, T. Maki, D. Yokoyama, H. Kumagai, Y. Hashimoto, T. Asari, H. Kawarada, Highly selective growth of vertically aligned double-walled carbon nanotubes by a controlled heating method and their electric double-layer capacitor properties. *Phys. Stat. Sol. (RRL)* **2**(2), 53–55 (2008)
119. L. Gao, A. Peng, Z.Y. Wang, H. Zhang, Z. Shi, Z. Gu, G. Cao, B. Ding, Growth of aligned carbon nanotube arrays on metallic substrate and its application to supercapacitors. *Solid State Commun.* **146**(9–10), 380–383 (2008)
120. H. Zhang, G. Cao, Z. Wang, Y. Yang, Z. Shi, Z. Gu, Tube-covering-tube nanostructured polyaniline/carbon nanotube array composite electrode with high capacitance and superior rate performance as well as good cycling stability. *Electrochem. Commun.* **10**(7), 1056–1059 (2008)
121. H. Zhang, G. Cao, Z. Wang, Y. Yang, Z. Shi, Growth of manganese oxide nanoflowers on vertically-aligned carbon nanotube arrays for high-rate electrochemical capacitive energy storage. *Nano Lett.* **8**(9), 2664–2668 (2008)
122. C.L. Pint, N.W. Nicholas, S. Xu, Z. Sun, J.M. Tour, H.K. Schmidt, R.G. Gordon, R.H. Hauge, Three dimensional solid-state supercapacitors from aligned single-walled carbon nanotube array templates. *Carbon* **49**(14), 4890–4897 (2011)
123. Z. Niu, W. Zhou, J. Chen, G. Feng, H. Li, W. Ma, J. Li, H. Dong, Y. Ren, D. Zhao, S. Xie, Compact-designed supercapacitors using free-standing single-walled carbon nanotube films. *Energy Environ. Sci.* **4**(4), 1440–1446 (2011)

124. A. Arun, H.L. Poche, T. Idda, D. Acquaviva, M.F.-B. Badia, P. Pantigny, P. Salet, A.M. Ionescu, Tunable MEMS capacitors using vertical carbon nanotube arrays grown on metal lines. *Nanotechnology* **22**(2), 025203 (2011)
125. S.R. Sivakkumar, D.-W. Kim, Polyaniline/carbon nanotube composite cathode for rechargeable lithium polymer batteries assembled with gel polymer electrolyte. *J. Electrochem. Soc.* **154**(2), A134–A139 (2007)
126. A.C. Dillon, K.M. Jones, T.A. Bekkedahl, C.H. Kiang, D.S. Bethune, M.J. Heben, Storage of hydrogen in single-walled carbon nanotubes. *Nature* **386**, 3770–3779 (1997)
127. Y. Ye, C.C. Ahn, C. Witham, B. Fultz, J. Liu, A.G. Rinzler, D. Colbert, K.A. Smith, R.E. Smalley, Hydrogen adsorption and cohesive energy of single-walled carbon nanotubes. *Appl. Phys. Lett.* **74**(16), 2307–2309 (1999)
128. C. Liu, Y.Y. Fan, M. Liu, H.T. Cong, H.M. Cheng, M.S. Dresselhaus, Hydrogen storage in single-walled carbon nanotubes at room temperature. *Science* **286**(5442), 1127–1129 (1999)
129. P. Chen, X. Wu, J. Lin, K.L. Tan, High H<sub>2</sub> uptake by alkali-doped carbon nanotubes under ambient pressure and moderate temperatures. *Science* **285**(5424), 91–93 (1999)
130. M.S. Dresselhaus, K.A. Williams, P.C. Eklund, Hydrogen adsorption in carbon materials. *MRS Bull.* **24**(11), 45 (1999)
131. G.G. Tibbetts, G.P. Meisner, C.H. Olk, Hydrogen storage capacity of carbon nanotubes, filaments, and vapor-grown fibers. *Carbon* **39**(15), 2291–2301 (2001)
132. M. Hirscher, M. Becher, M. Haluska, A. Quintel, V. Skakalova, Y.-M. Choi, U. Dettlaff-Weglikowska, S. Roth, I. Stepanek, P. Bernier, A. Leonhardt, J. Fink, Hydrogen storage in carbon nanostructures. *J. Alloys Compd.* **330–332**, 654–658 (2002)
133. C.C. Ahn, Y. Ye, B.V. Ratnakumar, C. Witham, J.R.C. Bowman, B. Fultz, Hydrogen desorption and adsorption measurements on graphite nanofibers. *Appl. Phys. Lett.* **73**(23), pp. 3378–3380 (1998)
134. P. Kim, C.M. Lieber, Nanotube nanotweezers. *Science* **286**(5447), 2148–2150 (1999)
135. R.H. Baughman, C. Cui, A.A. Zakhidov, Z. Iqbal, J.N. Barisci, G.M. Spinks, G.G. Wallace, A. Mazzoldi, D.D. Rossi, A.G. Rinzler, O. Jaschinski, S. Roth, M. Kertesz, Carbon nanotube actuators. *Science* **284**(5418), 1340–1344 (1999)
136. V.V. Deshpande, H.-Y. Chiu, H.W.C. Postma, C. Mikó, L. Forró, M. Bockrath, Carbon nanotube linear bearing nanoswitches. *Nano Lett.* **6**(6), 1092–1095 (2006)
137. U. Vohrer, I. Kolaric, M.H. Haque, S. Roth, U. Dettlaff-Weglikowska, Carbon nanotube sheets for the use as artificial muscles. *Carbon* **42**(5–6), 1159–1164 (2004)
138. S. Gupta, M. Hughes, A.H. Windle, J. Robertson, Charge transfer in carbon nanotube actuators investigated using in situ raman spectroscopy. *J. Appl. Phys.* **95**(4), 2038–2048 (2004)
139. V.H. Ebron, Z. Yang, D.J. Seyer, M.E. Kozlov, J. Oh, H. Xie, J. Razal, L.J. Hall, J.P. Ferraris, A.G. MacDiarmid, R.H. Baughman, Fuel-powered artificial muscles. *Science* **311**(5767), 1580–1583 (2006)
140. G. Spinks, G. Wallace, L. Fifield, L. Dalton, A. Mazzoldi, D. De Rossi, I. Khayrullin, R. Baughman, Pneumatic carbon nanotube actuators. *Adv. Mater.* **14**(23), 1728–1732 (2002)
141. S.V. Ahir, E.M. Terentjev, Photomechanical actuation in polymer-nanotube composites. *Nat. Mater.* **4**(6), 491–495 (2005)
142. A.R.T.S. Courty, J. Mine, E.M. Terentjev, Nematic elastomers with aligned carbon nanotubes: New electromechanical actuators. *Europhys. Lett.* **64**(5), 654–660 (2003)
143. H. Koerner, G. Price, N.A. Pearce, M. Alexander, R.A. Vaia, Remotely actuated polymer nanocomposites: stress-recovery of carbon-nanotube-filled thermoplastic elastomers. *Nat. Mater.* **3**, 115–120 (2004)
144. P. Miaudet, A. Derré, M. Maugey, C. Zakri, P.M. Piccione, R. Inoubli, P. Poulin, Shape and temperature memory of nanocomposites with broadened glass transition. *Science* **318**(5854), 1294–1296 (2007)
145. A.E. Aliev, J. Oh, M.E. Kozlov, A.A. Kuznetsov, S. Fang, A.F. Fonseca, R. Ovalle, M.D. Lima, M.H. Haque, Y.N. Gartstein, M. Zhang, A.A. Zakhidov, R.H. Baughman, Giant-stroke, superelastic carbon nanotube aerogel muscles. *Science* **323**(5921), 1575–1578 (2009)

146. P. Mérel, J.A. Kpetsu, C. Koechlin, S. Maine, R. Haidar, J. Pélouard, A. Sarkissian, M.I. Ionescu, X. Sun, P. Laou, S. Paradis, Infrared sensors based on multi-wall carbon nanotube films. *C. R. Phys.* **11**(5–6), 375–380 (2010)
147. K. Mizuno, J. Ishii, H. Kishida, Y. Hayamizu, S. Yasuda, D.N. Futaba, M. Yumura, K. Hata, A black body absorber from vertically aligned single-walled carbon nanotubes. *Proc. Natl. Acad. Sci. U S A* **106**(15), 6044–6047 (2009)
148. J.M. Xu, Highly ordered carbon nanotube arrays and IR detection. *Infrared Phys. Technol.* **42**(3–5), 485–491 (2001)
149. B.J. Hinds, N. Chopra, T. Rantell, R. Andrews, V. Gavalas, L.G. Bachas, Aligned multiwalled carbon nanotube membranes. *Science* **303**(5654), 62–65 (2004)
150. V.K.K. Upadhyayula, S.G. Deng, M.C. Mitchell, G.B. Smith, Application of carbon nanotube technology for removal of contaminants in drinking water: A review. *Sci. Total Environ.* **408**(1), 1–13 (2009)
151. B. Hinds, Dramatic transport properties of carbon nanotube membranes for a robust protein channel mimetic platform. *Curr. Opin. Solid St. M.* **16**(1), 1–9 (2011)
152. F. Du, L. Qu, Z. Xia, L. Feng, L. Dai, Membranes of vertically aligned superlong carbon nanotubes. *Langmuir* **27**(13), 8437–8443 (2011)
153. Y. Abdi, M. Khalilian, E. Arzi, Enhancement in photo-induced hydrophilicity of  $TiO_2$ /CNT nanostructures by applying voltage. *J. Phys. D: Appl. Phys.* **44**(25), 255405 (2011)
154. A. Arun, D. Acquaviva, M. Fernández-Bolaós, P. Salet, H. Le-Poche, P. Pantigny, T. Idda, A. Ionescu, Carbon nanotube vertical membranes for electrostatically actuated micro-electromechanical devices. *Microelectron. Eng.* **87**(5–8), 1281–1283 (2010)
155. A. Arun, S. Campidelli, A. Filoramo, V. Derycke, P. Salet, A.M. Ionescu, M.F. Goffman, SWNT array resonant gate MOS transistors. *Nanotechnology* **22**(5), 055204 (2011)
156. F.A. Ghavanini, P. Enoksson, S. Bengtsson, P. Lundgren, Vertically aligned carbon based varactors. *J. Appl. Phys.* **110**(2), 021101 (2011)
157. C.J. Hu, Y.H. Lin, C.W. Tang, M.Y. Tsai, W.K. Hsu, H.F. Kuo, ZnO-coated carbon nanotubes: Flexible piezoelectric generators. *Adv. Mater.* **23**(26), 2941–2945 (2011)
158. Y. Liu, I. Janowska, T. Romero, D. Edouard, L.D. Nguyen, O. Ersen, V. Keller, N. Keller, C. Pham-Huu, High surface-to-volume hybrid platelet reactor filled with catalytically grown vertically aligned carbon nanotubes. *Catal. Today* **150**(1–2), 133–139 (2010)
159. J. Luo, L.P. Mark, A.E. Giannakopoulos, A.W. Colburn, J.V. Macpherson, T. Drewello, P.J. Derrick, A.S. Teh, K.B. Teo, W.I. Milne, Field ionization using densely spaced arrays of nickel-tipped carbon nanotubes. *Chem. Phys. Lett.* **505**(4–6), 126–129 (2011)
160. K. Han, Y. Lee, D. Jun, S. Lee, K.W. Jung, S.S. Yang, Field emission ion source using a carbon nanotube array for micro time-of-flight mass spectrometer. *Jpn. J. Appl. Phys.* **50**(6), 06GM04, (2011)
161. B.K. Sarker, M.R. Islam, F. Alzubi, S.I. Khondaker, Fabrication of aligned carbon nanotube array electrodes for organic electronic devices. *Mater. Exp.* **1**(1), 80–85 (2011)
162. M. De Volder, S.H. Tawfik, D. Copic, A.J. Hart, Hydrogel-driven carbon nanotube micro-transducers. *Soft Matter* **7**(21), 9844–9847 (2011)
163. C. Yuana, C. Chang, Y. Song, Hazardous industrial gases identified using a novel polymer/MWNT composite resistance sensor array. *Mat. Sci. Eng. B: Solid* **176**(11), 821–829 (2011)
164. A. Di Bartolomeo, M. Sarno, F. Giubileo, C. Altavilla, L. Iemmo, S. Piano, F. Bobba, M. Longobardi, A. Scarfato, D. Sannino, A.M. Cucolo, P. Ciambelli, Multiwalled carbon nanotube films as small-sized temperature sensors. *J. Appl. Phys.* **105**, 064518 (2009)
165. C. Kocabas, H. sik Kim, T. Banks, J.A. Rogers, A.A. Pesetski, J.E. Baumgardner, S.V. Krishnaswamy, H. Zhang, Radio frequency analog electronics based on carbonnanotube transistors. *Proc. Natl. Acad. Sci. U S A* **105**(5), 1405–1409 (2008)